Specific Combinations of Physiological Tau Phosphorylation Regulate Tau-Microtubule Interactions in Developing Neurons

Nima N Naseri[1,2], Tian Xu[3], Sapanna Chantarawong[2], Steven M Patrie[3], Neil L Kelleher[3], Manu Sharma[4], Ophir Shalem[2,3], Elizabeth Rhoades[1,6]

[1]Department of Chemistry, University of Pennsylvania, Philadelphia, PA, USA

[2]Center for Cellular and Molecular Therapeutics, Children's Hospital of Philadelphia, Philadelphia, PA, USA

[3]Department of Chemistry, Northwestern University, Evanston, Illinois 60208, United States

[4]Appel Institute for Alzheimer's Research, and Feil Family Brain & Mind Research Institute, Weill Cornell Medicine, New York, NY, USA

[5]Department of Genetics, Perelman School of Medicine, University of Pennsylvania, Philadelphia, PA, USA

[6]Department of Biochemistry and Biophysics, Perelman School of Medicine, University of Pennsylvania, Philadelphia, PA, USA

ABSTRACT

Tau phosphorylation is a defining feature of Alzheimer's disease, yet it also plays an essential physiological role in stabilizing microtubules (MTs) during normal neuronal development. While individual phosphorylation sites have been well-studied in pathology, it remains largely unknown how combinatorial phosphorylation is regulated under physiological conditions. Here, we uncover distinct, site-specific phosphorylation patterns on tau in developing human neurons. With top-down mass spectrometry we find that functional, endogenous tau is highly modified, with up to 21 phosphates per molecule. We identify patterns of co-occurrence between phosphorylation sites that are in proximity in the linear protein sequence, such as epitopes S202/T205/T212/T217 and T231/S235/S262. Moreover, these phospho-epitopes define discrete pools of tau and regulate tau-MT interactions in coordination, providing a mechanism for fine-tuning the binding of tau to MTs. Intriguingly, we find that co-occurring phospho-epitopes are dynamically regulated in response to changes in MT integrity; chemical perturbation of neuronal MTs promotes rapid tau dephosphorylation by phosphatase PP2a at most sites to enhance tau-MT interactions and counteract destabilization. We then use the PS19 tauopathy mouse model to demonstrate that developmental and pathological tau phosphorylation patterns partially overlap, and that co-occurring phospho-epitopes exhibit similar associations with the insoluble fraction in aged mice. Our results reveal an isoform-dependence on the effects of site-specific tau phosphorylation on its behavior. Together, these findings define a combinatorial phosphorylation code that modulates tau's physiological function in neurons and raises the possibility that MT destabilization precedes tau phosphorylation in disease. This work provides a mechanistic framework for distinguishing functional from pathological tau phosphorylation, with implications for the development of therapies that specifically target disease-associated tau proteoforms.

INTRODUCTION

Hyper-phosphorylation of the microtubule (MT)- associated protein tau is strongly correlated with neuropathology in tauopathies including Alzheimer's disease (AD)[1-3]. Substantial evidence supports that tau's properties are significantly altered by post-translational modifications (PTMs) at specific residues, and that accumulation of these phosphate groups is found in intracellular deposits of aggregated tau. There is considerable discrepancy over whether any of these phospho-sites, of which there are over 80 potential sites in tau, are truly causative for aggregation[4] or merely correlated with disease progression. However, several sites are canonically associated with fibrillar aggregates found in disease. These include phosphorylation at sites primarily throughout the proline-rich region (PRR; comprised of domains P1 and P2) and the C-terminal domain at residues T181, S202, T205, T212, S214, T217, T231, S235, S262, S396, S404, S416 and S422 (**Fig. 1a**). Phosphorylation at sites T181 and T217 are currently the most precise tau biomarkers for AD diagnosis[5-8].

The relationship between tau phosphorylation and its physiological state is complex; in numerous organisms, including humans and rodents, tau is highly phosphorylated during normal fetal brain development, underscoring a functional, regulatory role for many phosphorylation sites[9-12]. In fact, many of the same phospho-

68 sites that are canonically associated with tau aggregates in disease are also present at this stage of
69 development, when phospho-tau (p-tau) is highly soluble and functional. Adding to the complexity is that there
70 are 6 tau isoforms expressed in the adult CNS. The shortest tau isoform, 0N3R (**Fig. 1a**), is exclusively expressed
71 in fetal tissue, whereas isoforms 0N3R, 0N4R, 1N3R and 1N4R comprise the majority of tau in adult brains[13].
72 However, much of the biochemical tau research has focused on the longest isoform, 2N4R, despite its relatively
73 low fraction in adult brains and negligible presence in fetal brains. The extent to which phospho-regulation of tau
74 function is isoform-dependent is underexplored, but may be particularly relevant in the fetal brain, as the
75 alternatively spliced regions are highly charged (net negative for N-terminal inserts, N; net positive for the repeat-
76 regions insert, R), and thus their inclusion/exclusion may be integral to the effects of negative charges or other
77 physico-chemical changes conferred by phosphorylation.

78 While the MT-binding domain (MBD) of tau has been the focus of intense research in promoting tau
79 aggregate assembly, the adjacent flanking PRR and R' domains are the primary regulatory regions of tau-MT
80 dynamics. The PRR is the most abundantly phosphorylated domain in tau[14]. As compared to the MBD, the PRR
81 is more competent in promoting MT assembly from soluble tubulin[15], and tau binding to both soluble tubulin and
82 MTs is greatly diminished by phospho-mimic mutations to the PRR[16,17]. The presence of the PRR is critical for
83 tau's ability to bind to MTs[18]; in fact, the MBD shows only weak affinity for MTs on its own[15,19]. Therefore, charge
84 alterations to the PRR by phosphorylation are highly regulatory to tau-MT interactions, likely in a site-specific
85 manner[20-22].

86 Broadly, phosphorylation to tau is thought to enhance its dissociation from MTs, or inhibit its binding to
87 growing MTs, to facilitate axonal outgrowth during development. Elevated levels of tau phosphorylation have
88 been observed in fetal human brains[11,12], supporting its physiological role in early neurodevelopment.
89 Experimental strategies to increase tau phosphorylation – such as *in vitro* incubation of recombinant tau with
90 kinases[23] or phosphatase inhibition via okadaic acid treatment[24] – can also induce high levels of tau
91 phosphorylation in non-neuronal cell culture models. However, these methods are generally non-specific to
92 phospho-epitopes in tau and may affect multiple substrates beyond tau. The complexity of tau phosphorylation
93 is underscored in its regulation through both physiological and pathological processes. For instance,
94 phosphorylation at one site may prime or enhance phosphorylation at additional sites, illustrating the coordinated
95 action of multiple PTMs to a single tau molecule[25-28]. In disease contexts, phosphorylation at specific residues,
96 such as S262 and S356, has been reported to exert opposing effects on tau's assembly into aggregates[29-32].
97 Such conflicting findings may reflect the influence of combinatorial PTMs rather than the effects of individual
98 phosphorylation events in isolation.

99 Beyond regulation of tau-MT interactions, some p-tau species have been suggested to localize to specific
100 cellular compartments[33-35]. However, there is unclarity in whether site-specific phosphorylation directs tau to
101 specific regions or instead tau is site-specifically modified in different regions. An alternative possibility is that
102 different p-tau species exist as distinct pools of proteins.

103 Here, we systematically characterize the role of site-specific phosphorylation in fetal tau using iPSC-

104 derived human neurons (i^3Neurons, referred to hereafter as iNeurons), which endogenously express high levels
105 of phosphorylated tau. We show that tau phosphorylation occurs not as isolated modifications but in co-regulated
106 combinations of specific sites. While phosphorylation is generally thought to diminish tau's interaction with MT,
107 our data reveal a reciprocal relationship in which MT destabilization triggers rapid, site-specific changes in tau
108 phosphorylation. These dynamic responses point to the existence of distinct pools of tau defined by their
109 combinatorial phospho-patterns. We then connect physiological regulation with disease states by comparing
110 these patterns in iNeurons with aged PS19 tauopathy mouse brains, uncovering both shared and divergent
111 features, including isoform-specific effects of phosphorylation and enrichment of co-occurring phospho-epitopes
112 in insoluble tau. Together, our findings suggest that combinatorial phosphorylation is not only a mechanism for
113 regulating tau function in healthy neurons, but also a potential driver of tau aggregation in disease.

114

115 # RESULTS

116 Throughout this study, we used validated antibodies against specific p-tau sites[36-38]. We also validated
117 these antibodies in mouse brains and human iNeurons by tau knockout and knockdown, respectively.

118 ***Tau is physiologically hyperphosphorylated in human iNeurons.***

119 Extensive phosphorylation to the fetal tau isoform, 0N3R, is reported in multiple organisms including
120 developing avians[9], rodents[10] and humans[11,12]. Based on this high abundance in fetal neurons from various
121 species, we postulated that a naïve neuronal model would be ideal for further exploring physiological tau
122 phosphorylation. Therefore, we turned to human iPSC-derived induced neurons (iNeurons), which suitably
123 recapitulate an embryonic environment[39-41], for our studies.

124 Numerous phosphorylation modifications to tau were readily detectable by Western blot in iNeurons,
125 which pre-dominantly express the fetal 0N3R isoform. Many canonical AD-relevant antibodies that we probed
126 were detected in iNeurons, including against sites pT181 (AT270 epitope), pS202/pT205 (AT8 epitope), pT212,
127 pT217, pT231 (AT180 epitope), pS235, pS262, pS396, pS404 and pS416 (**Fig. 1b**).

128 Despite exclusively using previously validated p-tau antibodies in this study, most have not been
129 specifically tested for tau reactivity in iNeurons. Additionally, iNeurons may express low levels of 1N3R and 2N3R
130 tau[42], limiting our ability to draw precise conclusions about the fetal 0N3R isoform. We overcame these limitations
131 by first generating a tau knockdown (tau^{KD}) iPSC model. We used CRISPR-interference to knockdown
132 endogenous tau in human Ngn2-iPSCs expressing dCas9-$KRAB_{(KOX1)}$ by transducing a sgRNA targeting *MAPT*
133 (tau^{KD} iPSCs). After neuronal differentiation, this approach resulted in near-complete tau depletion compared to
134 cells transduced with a non-targeting control (NTC) sgRNA (**Fig. S1a**). Unlike tau knockout models, tau
135 knockdown did not lead to compensatory upregulation of the MT-associated proteins (MAPs) MAP1A, MAP1B
136 or MAP2 (**Fig. S1b**). A key advantage of this tau^{KD} model is that individual tau isoforms can be re-introduced
137 post-differentiation via lentiviral transduction and titered to approximately endogenous levels (**Fig. S1c**), enabling

138 specific comparisons between tau isoforms without confounding compensation by other MAPs. Using this model,
139 we focused our investigation on the fetal 0N3R tau isoform in developing neurons. Importantly, p-tau antibody
140 specificity for tau was clearly demonstrated, apart from epitopes T212/S214, S214 (independently) and S422
141 (**Fig. S1d**). For the remainder of this study, we performed measurements in iNeurons either on endogenous tau
142 (3R) or used this exogenous isoform-specific model to facilitate comparisons of 0N3R vs 0N4R tau, as indicated.

143 The ease of p-tau detection in iNeurons intrigued us to explore the extent of phosphate addition per tau
144 molecule. We applied top-down mass spectrometry, which enables analysis of PTMs on intact proteins, to
145 quantify precise stoichiometries of phosphorylation of endogenous tau that was immunoprecipitated from
146 iNeurons. A mean of 12.2 and median of 12.0 phosphates per tau protein were detected. Phosphorylation levels
147 per tau molecule were quantitatively characterized by four distinct cluster groups: the first around 1-6 phosphates
148 per tau, the second around 7-10 phosphates per tau, the third around 11-18 phosphates per tau, and the fourth
149 around 19-21 phosphates per tau (**Fig. 1c** & **S2**). Within each cluster, the most frequent number of phospho-
150 modifications were 5, 8, 14 and 19 phosphates per tau. Additionally, acetylation was detected for tau molecules
151 modified with at least 11 but not fewer phosphates (**Fig. S2**). Based on past qualifiers that >7 phosphates per
152 tau protein are indicative of tau hyperphosphorylation[12], the high phosphorylation stoichiometries indicate that a
153 significant fraction, approximately 82%, of fetal tau is physiologically hyperphosphorylated in iNeurons. These
154 results reveal diverse populations of tau molecules that are phosphorylated in varying stoichiometries in
155 potentially distinct combinations.

156 We used an orthogonal approach, p-tau immunoprecipitation followed by back-calculation based on
157 immune-capture efficiencies, to estimate the frequency of site-specific phosphorylation to fetal tau in tau^{KD}
158 iNeurons expressing $0N3R^{EGFP}$. We asked the following question: when a quantifiable amount of tau is recovered
159 from a known amount of starting lysate, what percentage of that protein is positive for phosphorylation at the
160 captured phospho-epitope? To answer this question, we calculated the recovery of p-tau by immunoblotting using
161 a pan-tau antibody, and then normalized this value to the recovery of the immunoprecipitated phospho-site to
162 estimate the frequency of phosphorylation at that phospho-epitope[43]. In agreement with the top-down mass
163 spectrometry results, we estimated the phosphorylation frequency of several phospho-epitopes in 0N3R tau to
164 be as high as ~70%: Phospho-sites pT217 and pS235 were uncommon (<20%), pT181 and pT212 were
165 moderately common (>20%), and pS202/pT205, pT231 and pS396 were abundant (>45%) (**Fig. 1d**).

166 Together, these results demonstrate that phosphorylation to 0N3R tau is highly abundant in developing
167 iNeurons, underscoring the functional role for this regulatory modification during normal neuronal development.

168

169 ***Tau is phosphorylated in site-specific combinatorial patterns in iNeurons.***

170 Having identified high stoichiometries of tau phosphorylation in iNeurons, we next asked whether
171 phosphorylation patterns are random or occur in distinct combinations. A major caveat of using Western blots to
172 measure changes to phosphorylation levels in a protein of interest is that combinatorial PTMs at the single-

molecule level cannot be measured. Meanwhile, the regulation of tau-MT interactions may be dependent upon combinatorial phosphorylation to tau rather than single amino-acid modifications. Some combinations of phosphorylation have previously been observed in tau aggregates at epitopes such as S202/T205, T212/S214, T231/S235 and S396/S404[44-48]. However, combinatorial occurrences of tau phosphorylation are generally understudied, particularly in the physiological state. We reasoned that specific combinations of tau phosphorylation could be measured to predict specific fetal tau phospho-proteoforms.

To investigate potential co-occurrence of phosphorylation sites of tau in iNeurons, we asked: when tau is phosphorylated at a given site, what is the likelihood that it is also phosphorylated at a second site? To address this question, we examined tau's phosphorylation signature by immunoprecipitating p-tau at individual phospho-epitopes, followed by probing for co-occurring phosphorylation at additional sites (**Fig. 2a**). Immunoprecipitation was performed under denaturing conditions using site-specific p-tau antibodies targeting the most prominent AD-relevant epitopes within the PRR (T181, S202/T205, T212, T217 and T231) and one epitope in the C-terminus (S396). Immunoprecipitated p-tau was detected by Western blot, and co-occurring phosphorylation was assessed by co-blotting with a panel of p-tau antibodies spanning the PRR (T181, S202/T205, T212, T217, T231, S235), MBD (S262) and C-terminus (S396, S404, S416) (**Fig. 2b**). To estimate co-occurrence frequencies between two PTMs, the signal for each secondary phospho-site (normalized to input) was divided by the signal for the primary immunoprecipitated site (also normalized to input).

This approach yielded numerous unique patterns of co-occurring phospho-sites, indicating that tau phosphorylation follows non-random, site-specific patterns (**Fig. 2c**). First, we searched the dataset for previously reported co-occurrences to validate our approach. Consistent with earlier findings, two well-characterized co-occurrences, pS396/pS404 and pT231/pS235, were among the most frequently observed combinations. Specifically, phosphorylation at S396 was associated with a ~61% probability of concurrent phosphorylation at S404. Similarly, tau phosphorylated at T231 exhibited a ~41% likelihood of co-occurring phosphorylation at S235.

We next sought to identify novel patterns of tau phosphorylation by ranking the top ten most common pairwise co-occurrences (**Fig. 2d**, *left column*). From highest to lowest co-occurrence, the most prominent dual combinations of phospho-epitopes were as follows (with the immunoprecipitated site <u>underlined</u>): pS202/pT205/<u>pS396</u> (68%); <u>pS396</u>/pS404 (61%); <u>pS202/pT205</u>/pT212 (61%); pT181/<u>pS396</u> (58%); pT212/<u>pT217</u> (54%); pT181/<u>pS202/pT205</u> (52%); pT212/<u>pS396</u> (46%); pT181/<u>pT217</u> (45%); pT181/<u>pT231</u> (42%); <u>pT231</u>/pS235 (41%).

As an example, tau phosphorylated at T217 was also phosphorylated at T212 in ~54% of cases. Interestingly, the reverse relationship was not as prevalent: only ~8% of tau phosphorylated at T212 also carried phosphorylation at T217. Such asymmetric patterns suggest that phosphorylation at specific sites (e.g., T212) may act as a priming event for subsequent phosphorylation at a second epitope (e.g., T217), revealing potential hierarchical or sequential relationships among tau phosphorylation events.

Next, we explored this dataset to infer potential combinations of three simultaneous co-occurrences.

While two-dimensional matrices such as this one are informative for evaluating pairwise probabilities, they do not account for how a third site may influence, or be influenced by, an existing pair. For example, a high probability of co-occurrence between A and B [$P(A,B)$], and between B and C [$P(B,C)$], does not necessarily imply frequent co-occurrence of A, B and C together. To address this limitation, we applied minimum linkage analysis, a relatively conservative approach that estimates the probability of triple co-occurrence by using the weakest pairwise link among the three sites (i.e., $P(A,B,C)$=[minimum of $P(A,B)$, $P(A,C)$, $P(B,C)$]), to predict potential combinations of triplet PTMs. Using this metric, the top ten triplets were ranked from highest to lowest estimated co-occurrences to predict the most likely sets of three simultaneously co-occurring tau phospho-epitopes (**Fig. 2d**, *right column*). Some of the most frequent co-occurrences may indicate specific tau phospho-proteoforms (**Fig. 2e**).

The pairwise and triplet analyses revealed robust linkages between specific phospho-epitopes, which we subsequently grouped into functional clusters for the remainder of this study. Frequent co-occurrences were observed between S202/T205, T212 and T217, forming a tightly associated cluster (color-coded blue). A second cluster emerged linking T231 with S235 and S262 (color-coded red). In contrast, phosphorylation at T181 and S396 was broadly distributed, indicating more promiscuous co-occurrence patterns (color-coded gray). Finally, S404 and S416 co-occurred most strongly with S396, and to a lesser extent with T217 and T212, forming a distinct subgroup (color-coded magenta).

These patterns of co-occurrences suggest that tau phosphorylation is not a random process. The frequent co-occurrence of certain phospho-epitopes may reflect coordinated regulation by shared kinases or shared functional consequences in modulating tau's biochemical properties and behavior. Accordingly, we hypothesized that specific combinations of phosphorylation may define distinct pools of tau, each potentially associated with unique functional roles.

Site-specific phosphorylation to tau is associated with distinct pools of proteins.

Tau phosphorylation regulates tau-MT interactions, although molecular details are lacking for many individual phosphorylation sites, and combinatorial effects are even more poorly characterized. Given that different p-tau species were observed in unique phosphorylation combinations, we asked whether specific phospho-epitopes that exhibit high levels of co-occurrence exhibit similar sub-cellular localizations. We tested this hypothesis by fractionating MTs from iNeurons to assess whether specific phospho-epitopes are associated with MT-bound or cytosolic pools of tau.

We first separated pools of cytosolic MT-free tau from MT-bound tau by fractionating MTs from tau^{KD} iNeurons expressing the 0N3R isoform. Effective MT fractionation was indicated by separation of detyrosinated α-tubulin, a marker for intact MTs, from neuron-specific enolase (NSE), a marker for neuronal cytosol and plasma membrane (**Fig. 3a & S3**). Approximately 43% of tau and 77% of β-tubulin III was found in the MT-bound fraction (**Fig. 3b**). We then probed each fraction for p-tau to quantify the proportion of p-tau associated with the MT-bound pool (**Fig. 3b**).

We observed that tau phosphorylated at sites in the P2 domain of the PRR, proximal to the MBD (T231, S235), and in the R1 domain (S262) was found almost exclusively in the cytosolic fraction, while phosphorylation to the N-terminal segment of the P2 domain (sites S202/T205, T212 and T217) was more strongly associated with MTs. These localizations are consistent with the idea that the PRR can regulate tau-MT binding independently of the MBD. Phosphorylation in the P1 domain (T181) and C-terminal domain (sites S396, S404 and S416) was also more likely to be found in the MT fraction. Overall, we observed a bimodal distribution, in which tau that was phosphorylated outside of the last 15 residues of the P2 domain in the PRR + early MBD residues (T231, S235, S262) was more likely to be associated with the MT fraction compared to those within this region.

This bimodal effect was further emphasized by grouping phospho-epitopes with strong co-occurrence linkages together for a more convenient presentation of the data (**Fig. 3c**). As previously described, phospho-sites were categorized by the following color schematic: gray (T181, S396), blue (S202/T205, T212, T217), red (T231, S235, S262) and magenta (S404, S416). For clarity and consistency, we maintained this consolidated grouping throughout the remainder of the analyses. Data corresponding to each independent phospho-epitope are available in the supplementary information.

Overall, these findings indicate that tau that is phosphorylated at different phospho-epitopes is associated with distinct pools of MT-bound and cytosolic localizations.

Specific tau phospho-sites are co-regulated in response to MT damage and recovery.

We next asked whether the regulation of site-specific tau phosphorylation in iNeurons aligned with observed patterns of co-phosphorylation. Based on canonical models of tau-MT binding in neurodegeneration, phosphorylation to tau is thought to displace it from MTs, facilitating MT depolymerization. This line of reasoning seems counterintuitive in the context of developing neurons, which display high stoichiometries of tau phosphorylation while maintaining dynamic, elongating neurites comprised of polymerized MTs. Therefore, we considered an alternative hypothesis that phosphorylation to tau may also be influenced by the stability of MTs, rather than acting only as its primary regulator.

We tested this hypothesis by pharmacologically manipulating the neuronal cytoskeletal network using small molecules and assessed the impact on site-specific tau phosphorylation. MTs were destabilized using either nocodazole or demecolcine or stabilized using paclitaxel; as a control, actin filaments were depolymerized using latrunculin A (**Fig. 4a & S4a**). MT disruption with nocodazole or demecolcine led to pronounced tau dephosphorylation at numerous phospho-epitopes including S202/T205, T212 and T217, and more modest dephosphorylation at T231, S235 and S262. Intriguingly, MT disruption resulted in increased tau phosphorylation in the C-terminus at epitopes S404 and S416. MT stabilization with paclitaxel produced similar tau dephosphorylation patterns at epitopes S202/T205, T212, T217, though effects at T231, S235 and particularly S262 were less pronounced. In contrast, actin depolymerization had minimal impact on tau phosphorylation at

279 most of the measured epitopes (**Fig. S4b**). Together, these results suggest that site-specific tau phosphorylation
280 is differentially regulated in response to changes to MT stability.

281 We expanded upon this finding by measuring how phosphorylation to tau is modulated in response to
282 MT growth cycles. We induced MT catastrophe in iNeurons using a brief (5 minute) cold exposure followed by
283 either short- or long-term nocodazole treatment for 15 or 90 minutes, respectively, to analyze the cellular
284 response to acute versus sustained MT damage. The 90-minute nocodazole treatment group was followed by
285 washout and allowed to recover for either 1, 3 or 6 hours to test for site-specific regulation of tau phosphorylation
286 levels during re-stabilization of MTs (recovery phase) (**Fig. S5a**).

287 First, we measured the loss of MT stability during nocodazole treatment and after washout. Nocodazole
288 treatment disrupted the spindle-like cytoskeletal lattice that was clearly visualized in the control group but was
289 diminished by 90 minutes of treatment: Cytoskeletal spindles were detectable again in the soma by 3 hours after
290 nocodazole washout (**Fig. S5b**). The axonal localization of tau was also disrupted and recovered during this
291 same timeline. These visual findings were corroborated by immunoblot against detyrosinated α-tubulin and K40-
292 acetylated α-tubulin, markers of stable MTs, which were reduced to ~50% of control levels and recovered to
293 ~75% at 3 hours after nocodazole washout (**Fig. 4b,c**).

294 Next, we correlated changes to p-tau phosphorylation signatures throughout the treatment and recovery
295 periods with MT collapse and re-stabilization (**Fig. 4b,d** and **S5c**). Tau phosphorylation dynamics during MT
296 disruption and recovery could be classified into four distinct groups. The first group, comprised of T181 and S396
297 (gray line), was not significantly impacted by nocodazole treatment or washout. The second group (S202/T205,
298 T212, T217; blue line) underwent strong dephosphorylation (~23% of control levels) in response to nocodazole
299 treatment followed by rapid re-phosphorylation after nocodazole washout (recovery to ~64% of control levels).
300 The third group (T231, S235 and S262; red line) exhibited delayed and more modest dephosphorylation in
301 response to nocodazole treatment (~45% of control levels), with limited levels of re-phosphorylation after
302 nocodazole washout (recovery to ~54% of control levels). Phosphorylation at these six epitopes (S202/T205,
303 T212, T217, T231, S235, S262) continued to decrease until 1 hour into the recovery phase, even after
304 detyrosinated α-tubulin and acetylated α-tubulin levels had stabilized. More specifically, changes to phospho-
305 epitopes S202/T205, T212 and T217 closely mirrored the changes to MT stability throughout the time course,
306 while phosphorylation at epitopes T231, S235 and S262 exhibited similar but slower dephosphorylation and re-
307 phosphorylation trends. The rapidly dephosphorylated epitopes (S202/T205, T212 and T217) were more likely
308 to be bound to MTs than the more slowly dephosphorylated epitopes (T231, S235 and S262) (**Fig. S5d**). Lastly,
309 the fourth group included phospho-sites in the C-terminus (S404, S416; magenta line) which were conversely
310 rapidly phosphorylated within 15 min of MT collapse: phosphorylation at these sites continued to increase until
311 the nocodazole was washed out (~175% of control levels), at which point these sites were immediately, rapidly
312 dephosphorylated (~65% of control levels) in alignment with the timescale of MT stabilization, highlighting an
313 inverse relationship with MT integrity. The prompt increase in phosphorylation at these two epitopes may reflect
314 the importance of regulation at these sites for counteracting MT destabilization.

315 The patterns of site-specific dephosphorylation and phosphorylation in response to MT damage and
316 recovery corroborated the most prominent phosphorylation co-occurrences that were observed in iNeurons (from
317 **Fig. 2d**). For instance, pS202/pT205 and pT212 (~61% co-occurrence), pT212 and pT217 (~54% co-
318 occurrence), pT231 and pS235 (~41% co-occurrence), and pT181 and pS396 (~58% co-occurrence) were
319 similarly impacted by nocodazole treatment and washout. These coordinated changes support the notion that
320 these sites are not only frequently co-phosphorylated but also co-regulated in response to shifts in MT stability.

321 Although nocodazole treatment did not impact total (pan) tau or β-tubulin III levels, both proteins were
322 non-significantly upregulated after nocodazole washout, suggesting a potential compensatory cellular response
323 to counteract MT destabilization by increasing tau and tubulin levels (**Fig. 4b,c**). Notably, changes to tau
324 phosphorylation occurred prior to this upregulation; therefore, the observed patterns of dephosphorylation and
325 phosphorylation were independent of new protein translation.

326 In conjunction with our previous MT-fractionation data, the unique patterns of site-specific
327 dephosphorylation in response to MT growth cycles suggest that dephosphorylation of a subset of sites is most
328 critical to tau to binding to MTs to counteract effects of destabilization. While phosphorylation at sites T181, S396,
329 S202/T205, T212 and T217 remained unchanged or quickly recovered during MT recovery, sites T231, S235
330 and S262 were likely sustained in the dephosphorylated state to support MT re-stabilization. These data highlight
331 a critical role for phosphorylation at sites T231, S235 and S262 in regulating tau's interaction with MTs during
332 recovery. In contrast, the immediate phosphorylation increases at S404 and S416 suggest that these
333 modifications may promote or stabilize tau's association with MTs. More broadly, our data show that site-specific
334 tau phosphorylation is dynamically regulated by MT stability in distinct combinatorial patterns, with co-regulated
335 clusters including T181-S396, S202/T205-T212-T217, T231-S235-S262 and S404-S416.

336

337 ***Tau dephosphorylation by PP2a is necessary to stabilize shrinking MTs.***

338 These biochemical assays suggest that there are distinct pools of p-tau in developing neurons. As MTs
339 undergo collapse, specific p-tau sites are dephosphorylated, shifting the equilibrium toward increased tau binding
340 to MTs, potentially as a compensatory mechanism to counteract MT catastrophe. As cellular conditions become
341 conducive to MT regrowth or repair, these same sites are re-phosphorylated, tipping the balance back toward
342 less MT-bound tau and restoring dynamic flexibility. This regulatory model contrasts with the prevailing view in
343 neurodegeneration that phosphorylation to tau is thought to drive MT destabilization by disrupting tau's MT-
344 binding capacity. Our findings instead raise the possibility that, at least in the context of development, changes
345 in MT stability precede and influence site-specific tau phosphorylation. Taken together, these observations
346 suggest that tau phosphorylation can function both as a consequence and a driver of MT stability, with the
347 directionality of this relationship potentially differing between physiological and pathological states.

348 We tested this hypothesis by manipulating the molecular pathways that regulate tau dephosphorylation
349 and phosphorylation during MT collapse and regrowth. Thus, we sought to identify the phosphatases and kinases

350 that are activated during this process. First, we measured phosphatase and kinase activation for enzymes that
351 have been previously implicated in tau regulation[10,25]. We found that the phosphatase PP2a was activated during
352 nocodazole treatment, concurrent with the period of tau dephosphorylation (**Fig. 5a & S6**, *top panel for each*).
353 The kinases Erk1/2 and Akt1 were activated after nocodazole washout, aligning with the period of tau re-
354 phosphorylation (**Fig. 5a & S6**, *middle two panels for each*), whereas the kinase GSK3β was activated as soon
355 as 15 minutes after nocodazole treatment (**Fig. 5a & S6**, *bottom panel for each*), preceding the period of
356 phosphorylation of most tau sites except for S404 and S416.

357 Next, we tested the functional consequences of tau dephosphorylation and re-phosphorylation on MT
358 stability by pharmacologically modulating phosphatase and kinase activity. We combined phosphatase inhibition
359 with nocodazole treatment to assess the role of tau dephosphorylation during MT collapse, and applied kinase
360 inhibition during the recovery period to test for the impact of blocking tau phosphorylation during MT recovery.
361 Among the kinase inhibitors that we tested – targeting Akt1 (AKT1 inhibitor VIII), Erk1/2 (Erk1/2 inhibitor I) and
362 GSK3β (BIO) – only the Akt1 inhibitor was both effective and selective for its intended target in iNeurons during
363 the tested timeline (**Fig. S7a,b**). Akt1 inhibition resulted in only a modest improvement in MT stability compared
364 to DMSO treatment (**Fig. S7b**), suggesting that blocking tau phosphorylation at sites that are targeted by Akt1
365 during MT recovery has a limited effect on MT stabilization. These findings imply that blocking tau
366 dephosphorylation during MT collapse may play a more critical role in maintaining MT integrity.

367 In support, phosphatase inhibition during MT collapse had a dramatic effect on MT stability. We tested
368 two small pharmacological inhibitors of PP2a, LB-100 (reversible) and Calyculin A (irreversible), to inhibit PP2a
369 activity during nocodazole treatment for 90 minutes. Following treatment, both nocodazole and the inhibitors
370 were washed out, and cells were allowed to recover for 3 hours. Successful PP2a inhibition was confirmed by
371 anti-pPP2a immunoblot (**Fig. 5b**). LB-100 treatment reduced MT stability compared to DMSO, but MTs were able
372 to recover after washout (**Fig. 5b-d**). In contrast, treatment with the potent PP1/PP2a inhibitor Calyculin A led to
373 severe MT destabilization, and they were not able to recover after washout due to the irreversible nature of
374 inhibition.

375 We correlated these changes in MT stability with tau phosphorylation by measuring the impact of PP2a
376 inhibition on tau's phosphorylation state during nocodazole treatment. We compared mild inhibition by LB-100
377 with potent inhibition by Calyculin A to tease out specific tau phospho-epitopes that may be critical for stabilizing
378 shrinking MTs. As expected, PP2a inhibition correlated with reduced dephosphorylation at multiple phospho-
379 epitopes, including S202/T205, T212, T217, T231, S235 and S262, while phosphorylation at T181, S396, S404
380 and S416 remained largely unaffected (**Fig. 5c,e & S8**). Of note, Calyculin A treatment resulted in dramatically
381 higher levels of phosphorylation at phospho-epitopes T212, S235, and especially at S262, reinforcing that
382 dephosphorylation of these residues is critical for tau's capacity to stabilize shrinking MTs.

383

384 ***Phospho-tau is abundant and soluble in developing mouse brains.***

385 Our findings on the combinatorial regulation of physiological tau phosphorylation patterns in iNeurons
386 motivated us to compare our results with previous studies in other system models. We asked how similar tau
387 phosphorylation modifications are between the developmental and pathological states, as others have done[10-
388 12]. Therefore, we turned to wildtype and PS19 tauopathy mouse models to further investigate the nature of fetal
389 tau phosphorylation *in vivo*.

390 First, we probed for site-specific tau phosphorylation during embryonic development by dissecting
391 wildtype embryonic mouse brains at 12 days post-gestation (embryonic day 12, or *E12*). As reported by others,
392 we observed robust immunoreactivity for several canonical AD-relevant p-tau epitopes, including S202/T205,
393 T231, S235, S262, S396, S404, S416 and S422 (**Fig. 6a**). To investigate the subcellular distribution of p-tau, we
394 focused on pS404, which was readily detectable in primary neuron cultures derived from wildtype embryonic
395 mouse brains (**Fig. 6b**). Notably, the localization patterns for pS404 and α-tubulin were extremely similar,
396 suggesting that, as in iNeurons, tau that is phosphorylated at S404 remains capable of associating with MTs.

397 Next, we asked how p-tau levels change over the course of aging. An aging time course of wildtype mice
398 revealed that pan-tau levels were ~20-fold higher at P0 compared to 1-year-old mice (**Fig. 6c**). A modest band
399 shift in pan-tau signal at P0 to P31 and onwards likely represents an isoform switch from highly phosphorylated
400 3R to less phosphorylated 4R tau. The band shift representing isoform switching was more prominent when we
401 probed for changes to several phospho-sites. When normalized to pan-tau levels, several of these phospho-
402 sites were most highly enriched at post-natal day 0 (P0), while some sites such as pS202/pT205, pT231 and
403 pS396 were bimodally expressed at birth and again at 1-year of age, but less so in between. Overall, these data
404 are aligned with the presence of physiological tau phosphorylation in developing brains and are consistent with
405 prior studies in rats, avians and humans.

406 In contrast to the age-dependent decline in total and p-tau levels observed in wildtype mice, tauopathies
407 such as AD are characterized by an aberrant, age-related increase in p-tau. This distinction prompted us to
408 compare site-specific phosphorylation patterns of tau between fetal mouse brains – representing a
409 developmental stage with physiologically high levels of tau phosphorylation – and aged tauopathy mouse brains
410 – a time when tau phosphorylation is largely ectopic. For this comparison, we utilized the PS19 tauopathy mouse
411 model, which overexpresses the 1N4R isoform of tau harboring the pathogenic P301S mutation and is well-
412 documented to develop insoluble tau deposits by 3 months of age[49]. Given that tau phosphorylation is frequently
413 used as a marker of its aggregation in AD, we also examined whether p-tau forms insoluble deposits in neonatal
414 PS19 mouse brains (P0) and compared them to 9-month-old PS19 mice. To this end, we assessed the levels
415 and solubility of p-tau across numerous phospho-epitopes at these two timepoints by fractionating soluble and
416 insoluble proteins and probing them using a panel of 11 site-specific p-tau antibodies (**Fig. 6d**).

417 We first compared p-tau levels, normalized to pan-tau, between the neonate and aged PS19 mice (**Fig.
418 6d,e**). In contrast to aged WT mice, numerous p-tau epitopes were readily detectable in aged PS19 mice, and a
419 clear mass shift was evident between 0N3R mouse tau at P0 compared to 1N4R human tau at 9-months.
420 Phosphorylation at sites T212/S214 (AT100 epitope) and S235 was barely detectable at P0 but showed a non-

421 significant >3-fold increase and a significant >4-fold increase, respectively, by 9-months of age. In contrast,
422 phosphorylation levels, normalized to pan-tau, in the 9-month-old PS19 mice were a fraction of those found in
423 neonates at several phospho-epitopes including at sites S202/T205 (~93% lower), T231 (~72% lower), S262
424 (~64% lower) and S396 (~70% lower). No significant differences in tau phosphorylation, normalized to pan-tau,
425 were observed between P0 and 9-month-old PS19 mice at phospho-sites T181, T217, S404, S416 or S422,
426 suggesting comparable phosphate occupancy at these sites across both timepoints. Together, these results
427 highlight conserved and divergent patterns of tau phosphorylation that may distinguish physiological from
428 pathological modifications.

429 We next evaluated the solubility of p-tau across developmental and pathological time points. In both P0
430 and 9-month-old PS19 mice, the majority of pan-tau (anti-Tau5) was recovered in the soluble fraction (**Fig. 6d,f**).
431 The high percentage of pan-tau solubility observed in the aged mice likely reflects the considerable
432 overexpression of tau in this transgenic model, because >4-fold more pan-tau was found in the insoluble fraction
433 in the 9-month-old compared to neonatal PS19 mouse brains. Substantial differences in p-tau solubility were
434 evident between neonatal and 9-month-old brains. In aged mice, several phospho-epitopes were predominantly
435 associated with the insoluble fraction, especially at phospho-epitopes S202/T205 (~61% soluble), T212/S214
436 (~33% soluble), T217 (~50% soluble) and strikingly at S422 (~17% soluble). Additional phospho-sites such as
437 T181 (~82% soluble), T231 (~75% soluble), S235 (~84% soluble) and S262 (~75% soluble) also showed greater
438 association with the insoluble fraction with age. In contrast, phosphorylation at C-terminal sites S396 (~94%
439 soluble), S404 (~91% soluble) and S416 (~94% soluble) remained largely in the soluble pool. In the 9-month-
440 old mice, the insoluble p-tau band was not infrequently mass-shifted upwards compared to the soluble p-tau
441 signal, suggesting these higher bands may represent more heavily modified insoluble tau species. Notably, in
442 neonatal brains, nearly all p-tau species examined were exclusively found in the soluble fraction, without any
443 evident mass shifts between the soluble and insoluble fractions.

444 These data indicate that while there are many overlaps between physiological and disease-associated
445 tau phosphorylation signatures, fetal p-tau does not form aggregates. This divergence between developmental
446 (i.e., physiological) phosphorylation in the fetal brain and ectopic phosphorylation during aging may give rise to
447 distinct p-tau species, some of which may be unique to either state.

448

449 ***Site-specific phosphorylation has differential effects on different tau isoforms.***

450 Our data demonstrates that fetal tau is modified at many of the same phospho-epitopes as pathology-
451 associated tau, and in some cases even more so, yet fetal tau does not form insoluble aggregates. A key
452 distinction between neonatal and adult tau lies in their isoform composition: neonates exclusively express 3R
453 tau, while adults express both 3R and the more positively charged 4R isoform. Importantly, 4R tau is not present
454 during early development, when tau phosphorylation levels are highest, suggesting that the regulatory
455 environment governing tau phosphorylation shifts as the brain matures. This age-dependent shift in tau isoform
456 expression raises the possibility that site-specific phosphorylation may have different functional consequences

457 for 3R and 4R tau, potentially driven by differences in their intrinsic charges and by the age-context in which they
458 are expressed.

459 One notable shortcoming of iNeurons is their inability to recapitulate the developmental transition from
460 3R to 4R tau following neuronal maturation[42]. To address this limitation, we returned to the tau^{KD} model that we
461 generated earlier and lentivirally expressed a comparable isoform, 0N4R tau, to approximately endogenous
462 levels (**Fig. S1c**). This system allowed us to directly compare the phospho-site-specific interactions of 4R tau
463 with MTs, and to draw parallels to our earlier findings in 3R tau.

464 Using this model, we first validated that 0N3R and 0N4R tau displayed comparable levels of
465 phosphorylation in the fetal iNeuron environment. Across most epitopes, phosphorylation levels were similar
466 between the two isoforms, except at T231 and S235 (**Fig. S9a**), which were phosphorylated at lower levels in
467 0N4R compared to 0N3R tau. Importantly, these trends were independent of total tau expression levels for each
468 isoform.

469 We next asked whether phosphorylation at these sites differently impacted 3R and 4R tau's association
470 with MTs. Thus, we fractionated MTs from tau^{KD} iNeurons expressing 0N4R tau and quantified the MT-bound
471 and cytosolic pools of p-tau, making direct comparisons to our previously established measurements for 0N3R
472 tau (**Fig. 7a**). Although the percentage of MT-bound tau was equivalent for both 0N3R and 0N4R (~43 vs ~48%,
473 respectively), phospho-0N4R was consistently more enriched in the MT fraction across nearly all epitopes (**Fig.
474 7a** and **Fig. S9b-d**). This difference was most dramatic at sites T217 and T231, where >2-fold more 0N4R tau
475 was found in the MT-bound pool compared to 0N3R tau. Strikingly, more than 50% of phospho-0N4R tau was
476 bound to MTs when phosphorylated at T181, S202/T205, T212, S396, S404 and S416, indicating that
477 phosphorylation at these sites either is not as disruptive or may even enhance rather than diminish binding of
478 0N4R to MTs.

479 These findings suggest that 0N3R is more sensitive to phosphorylation at the same epitopes in terms of
480 disrupting MT binding, whereas 0N4R tau retains some degree of its MT association despite phosphorylation at
481 the same epitopes. The observed differences in MT binding between 0N3R p-tau and 0N4R p-tau appear two-
482 fold: First, cytosolic pools of 0N3R p-tau were generally higher than those of 0N4R p-tau (**Fig. S9c**): Second,
483 MT-bound pools of 0N4R p-tau exceeded those of 0N3R p-tau (**Fig. S9d**). In particular, pT231 and pS235 were
484 reduced in the cytosolic fraction for 0N4R compared to 0N3R, while pT212, pT217 and pT231 were increased
485 in the MT-bound fraction for 0N4R compared to 0N3R.

486 To directly test whether isoform-dependent effects of site-specific tau phosphorylation influence MT
487 dynamics, we turned to a cell-free system to model and validate these interactions biophysically. While phospho-
488 mimetic substitutions are widely used, their ability to accurately mimic endogenous phosphorylation remains
489 uncertain. To address this, we performed recombinant MT polymerization assays using wildtype and a panel of
490 site-specific phospho-mimetic variants of 0N3R and 0N4R tau. We cloned, expressed and purified recombinant
491 forms of wildtype 0N3R and 0N4R tau, along with phospho-mimetic mutants generated via Thr>Glu or Ser>Glu
492 substitutions at key sites identified from our neuronal dataset: T181, T217, T231, S235, S262, S396 and S404.

493 As independent phospho-mimetics do not account for combinatorial phosphorylation modifications, we
494 additionally generated three combinatorial phospho-mimetics based on the observed patterns in neurons:
495 T231E/S235E, T231E/S262E and S396E/S404E.

496 Using purified soluble tubulin from bovine brains, we assessed the capacity of each tau variant to promote
497 polymerization of soluble tubulin (**Fig. 7b**). Overall, most single-site phospho-mimetics impaired MT
498 polymerization compared to their wildtype counterparts, regardless of isoform. A notable exception was the
499 S262E mutation, which severely impaired the rate of MT polymerization by ~73% in 0N3R tau but had little to no
500 effect on 0N4R tau. Combinatorial phospho-mimetics revealed further divergent effects in the two tau isoforms.
501 The dual mutants T231E/S235E and T231E/S262E, which were identified by our co-linkage and co-regulation
502 analyses, markedly impaired MT polymerization activity by 0N3R but less so by 0N4R tau (**Fig. S10**). Although
503 individual mutations at T231E and S235E similarly reduced MT polymerization activity across both isoforms,
504 their combination (T231E/S235E) had an additive inhibitory effect on 0N3R's but not 0N4R's abilities to promote
505 MT polymerization. Consistent with our observations in neurons, phospho-mimetic mutations at S396E, S404E
506 and in combination had comparatively modest effects on MT polymerization by either tau isoform. These findings
507 are in concurrence with our neuronal data, indicating that 0N3R is more sensitive to the inhibitory effects of
508 phosphorylation than 0N4R tau, particularly at sites S262E and in multi-site phospho-mimetic contexts. In
509 support, correlation of p-tau bound to MTs (from iNeurons) with MT polymerization rates (from recombinant
510 proteins) emphasized a clear disruption by site-specific phosphorylation/phospho-mimics to 0N3R's (R^2=0.480)
511 but not 0N4R's (R^2=0.002) interaction with MTs (**Fig. 7c**).

512

513 # DISCUSSION

514 PTMs like phosphorylation diversify the functions of proteins, yet they are often studied in isolation. Tau
515 is a striking example of PTM complexity, with over 80 potential phosphorylation and 40+ potential acetylation
516 sites, as well as additional modifications including methylation, ubiquitination, succinylation, *O*-GlcNAcylation
517 and others[14,50-52]. Our study explores the combinatorial landscape of tau phosphorylation in a physiological
518 context – one that may serve as a critical reference point to tau's behavior in disease. Future studies identifying
519 specific phospho-proteoforms in physiological and pathological contexts could reveal tau molecules that are
520 unique to the disease state.

521 For instance, by extending our analysis to aged wildtype and PS19 tauopathy mouse brains, we found
522 that while absolute phosphorylation levels and isoform expression differ, patterns of co-regulated phospho-sites
523 in iNeurons mirrored those found in insoluble tau fractions in aged PS19 mice (**Fig. 7d**). This raises the intriguing
524 possibility that combinatorial phospho-regulation contributes not only to MT association, but also aggregation
525 propensity in disease. While the comparison spans different isoforms – primarily 0N3R mouse tau in neonates
526 versus predominantly 1N4R^{P301S} human tau in aged PS19 mice – this is unlikely to confound our interpretation,
527 as mouse and human tau share ~97.8% amino acid homology between T181 and the C-terminus, conserving

528 all phospho-sites probed in this study.

529 From the physiological perspective, we used iPSC-derived human neurons to show that endogenous
530 fetal tau is extensively phosphorylated, with up to 21 phosphate groups per molecule as measured by top-down
531 mass spectrometry – far exceeding prior estimates from fetal or AD brains[12,24,53,54]. Interestingly, a prior study
532 similarly identified two pools of p-tau centered around ~8 and ~14 phosphates per tau molecule, by utilizing
533 2N4R overexpression in insect cells[24]. However, in that study and in contrast to our current work, the cells were
534 pre-treated with phosphatase inhibitors prior to lysis to enrich p-tau; meanwhile, our results support a natural
535 higher level of p-tau in developing human neurons. Importantly, we identified that specific combinations of
536 phospho-sites are co-regulated, shifting in response to changes in MT stability. The exact kinases that target
537 each specific epitope in the context of a developing neuron are uncertain, though past studies have found that
538 numerous kinases, such as family proteins in the GSK3, CDK, ERK, JNK, p38, MAPK and other pathways, can
539 target multiple and often overlapping phospho-epitopes in tau[25,55-57]. These identified phospho-patterns appear
540 to define discrete tau proteoforms with distinct MT-binding properties, challenging the notion that phosphorylation
541 broadly reduces tau's MT association.

542 In developing neurons, tau phosphorylation appears responsive to MT growth cycles (**Fig. 8**). When MTs
543 destabilize, such as during the frequent collapse and regrowth cycles of axons, the first pool of p-tau species,
544 phosphorylated at S202/T205, T212 and T217, are dephosphorylated presumably to enhance tau's binding
545 capacity to tubulin/MTs. Then, a second pool of p-tau species (i.e., pT231, pS235, pS262) is dephosphorylated
546 to promote further MT stabilization. Based on our MT fractionation measurements for each phospho-epitope, the
547 rapid dephosphorylation of the first set of sites (S202/T205, T212 and T217) may indicate a cellular response to
548 increase the affinity of p-tau species which are already bound to MTs. Meanwhile, the slower dephosphorylation
549 of the second set of phospho-epitopes (T231, S235 and S262) may represent dephosphorylation of a
550 cytoplasmic fraction of tau, thus contributing to the overall population of dephosphorylated tau that is available
551 to promote MT growth and repair. Among the phospho-sites measured in this study, dephosphorylation at sites
552 T231, S235 and S262 appear to be the most critical for enhancing this interaction. Once MT stability is re-
553 established, these same sites are re-phosphorylated: first, epitopes S202/T205, T212 and T217 are
554 phosphorylated, possibly to facilitate dissociation of tau from MTs: then, tau is re-phosphorylated at sites that
555 strongly inhibit tau's binding to MTs (e.g., T231, S235 and S262) in order to maintain cytosolic pools of p-tau that
556 are dissociated from MTs. This paradigm contrasts with the prevailing view in neurodegeneration, where
557 increased tau phosphorylation is thought to cause MT destabilization. Our findings suggest a more nuanced
558 relationship: in physiological settings, tau phosphorylation responds to cytoskeletal changes, while in disease,
559 the inverse may occur – or both directions may be active in a pathological feedback loop.

560 Isoform composition further shapes tau's phospho-responsiveness. We show that 0N3R tau is more
561 sensitive than 0N4R tau to the inhibitory effects of specific phosphorylation sites on MT polymerization and
562 localization. In particular, dual phospho-mimetics (e.g., T231E/S235E, T231E/S262E) strongly suppress MT
563 polymerization by 0N3R but not 0N4R tau. This differential susceptibility may reflect an important developmental
564 switch: phosphorylation serves a regulatory role in 3R-dominant fetal tau, while the emergence of 4R tau in the

maturing brain may buffer tau's response to PTMs, or allow more fine-tuning of tau function, unless it is overwhelmed as in disease.

Our findings point to multiple layers of phospho-regulation that govern tau's function: site-specific, combinatorial and isoform-dependent. Many questions remain about how combinatorial tau phosphorylation is regulated and how it influences tau's diverse functions. Most of the pairwise and triplet phospho-combinations we identified are novel, leaving open how, when and where these phospho-proteoforms arise in neurons, and what roles they play beyond regulating tubulin/MT interactions. The diversity of phospho-proteoforms may allow tau to carry out distinct cellular roles, including MT regulation, tubulin-actin crosslinking, vesicle trafficking, or synaptic modulation, depending on its modification profile.

Importantly, our study has limitations. Phospho-specific antibodies may vary in affinity and can be affected by neighboring modifications, which may lead to underestimation of phospho-occupancy at certain sites. For example, T181 phosphorylation frequently co-occurred with other phospho-sites while also exhibiting high levels of independent phosphorylation, yet we estimated its occupancy at only ~35%. Another limitation is that the use of kinase/phosphatase inhibitors and cytoskeleton-targeting small molecules are non-specific, and may affect tau indirectly, outside of physiological pathways that normally modify MT stability. Future work using genetic approaches to modify trans-regulators of tau-MT interactions, high-resolution top-down proteomics or genetic code-expansion strategies to incorporate site-specific PTMs, could more precisely resolve how phospho-proteoforms are regulated and function.

As a whole, our results demonstrate that while fetal tau is extensively phosphorylated at many of the same sites implicated in tauopathy, it remains functionally distinct due to its isoform composition and differential sensitivity to phosphorylation. Compared to 0N4R tau, 0N3R tau exhibits a greater sensitivity to phospho-mediated disruption of MT interactions, suggesting that its role during early brain development involves finely tuned regulation by phosphorylation. The increased susceptibility of 0N3R tau to phospho-regulation may underlie its unique role during early neuronal development, when dynamic modulation of MT interactions is essential. Our findings underscore the importance of both combinations of site-specific phosphorylation patterns and isoform context in modulating tau function. Furthermore, the differential behavior of 0N3R versus oN4R tau in response to phosphorylation highlights a critical layer of regulation that may contribute to isoform-specific vulnerabilities observed in tauopathies.

In summary, we demonstrate that physiological tau phospho-proteoforms are tightly linked to MT dynamics, sensitive to isoform context, and organized in co-regulated clusters that may foreshadow aggregation behavior in disease. These insights reframe our understanding of tau regulation and highlight new avenues for exploring how phosphorylation contributes to tau function and dysfunction.

METHODS

Mouse lines and husbandry

Ethical Statement: All animal procedures including husbandry and experimental procedures, were performed according to NIH guidelines and approved by the Institutional Animal Care and Use Committee at Weill Cornell Medicine (Animal Welfare Federal Wide Assurance No: A3290-01; protocol number 2014-0015).

Mouse strains: PS19 mice[58] overexpressing human tau (1N4R) carrying the disease-causing P301S mutation, driven by the mouse prion protein promoter (stock# 008169, Jackson Lab, ME) and wildtype (C57BL/6 J; Stock # 000664 Jackson Labs, ME) were kept in 12 h light/dark cycle in a temperature-controlled room with free access to water and food. PS19 transgenic mice (generated in C57BL/6 background, and inbred for >20 generations) were bred to wildtype mice of the same line to generate 50% transgenic and 50% wildtype offspring used in this study. Littermates were raised together and tissue were harvested in parallel.

Mouse tissue harvesting

Mouse brains were dissected, washed once with ice-cold PBS, and cut into left and right hemispheres. The brains were flash-frozen in under 60 seconds post-decapitation. For post-natal brain dissections, one hemisphere was immediately flash-frozen in liquid nitrogen and stored at -80C for solubility assays. The other hemisphere was immediately resuspended to 10% (w/v) in PBS supplemented with protease and phosphatase inhibitors, mechanically homogenized using a dounce tissue grinder, and supplemented with 4x Laemmli buffer (supplemented with 10 mM DTT). The same homogenization protocol was used for embryonic brain dissections (E12). These samples were stored at -80C to be used for SDS-PAGE followed by immunoblot.

Primary neuron cultures

Primary neurons from embryonic day 12 wildtype mice were cultured essentially as previously described[59]. Briefly, cortices were dissected in ice-cold HBSS followed by trypsinization (0.05% trypsin-EDTA) for 10 min at 37 °C. The brains were then triturated with a siliconized pipette and plated onto poly-L-lysine coated glass coverslips. Plating medium (DMEM, Thermo Fisher) containing 5 g/L glucose, 0.2 g/L $NaHCO_3$, 0.1 g/L transferrin, 0.25 g/L insulin, 0.3 g/L L-glutamine, and 10% fetal bovine serum was replaced with growth medium (DMEM, Thermo Fisher) containing 5 g/L glucose, 0.2 g/L $NaHCO_3$, 0.1 g/L transferrin, 0.3 g/L L-glutamine, 5% fetal bovine serum, 2% B-27 or N21-MAX supplement, and 2 μM cytosine arabinoside 2 days after plating. On day *in vitro* 8, cultured neurons were washed twice with cold PBS and fixed with 4% PFA (in PBS) for 20 minutes at room temperature, followed by immunofluorescence.

Generation of tau^{KD} human iPSCs

Human WTC11 iPSCs stably-expressing Ngn2 (under a dox-inducible promoter) and dCas9-KRAB$_{(KOX1)}$ were transduced with sgRNAs targeting *MAPT* followed by puromycin selection. Three sgRNAs were tested independently: 1) 5'GTGTTGGTGCCGGAGCTGGT, 2) 5'GGGCTGCAGTCGAGAGTGAA, and 3) 5'GGAAGCCCCAGTCTGCGGAG. Non-targeting control (NTC) sgRNA: 5' GCCGAGCGGCAGGGTGCCGC. The first sgRNA resulted in stable knockdown of tau protein for at least 45 days post-differentiation while the other two sgRNAs resulted in only partial tau knockdown. The described experiments were performed using iPSCs generated from the first sgRNA, referred to as tau^{KD}, for lentiviral transduction of tau constructs.

Lentivirus production and transduction

Lentivirus was generated as previously described[59]. Briefly, HEK293T cells were co-transfected at low passage with 1.06μg of pMDLG (Addgene plasmid# 12251), 0.57μg of pMD2.G (Addgene plasmid# 12259), 0.4μg of pRSV-Rev (Addgene plasmid# 12253) plasmid, and 1.6μg of the lentiviral plasmid, using 1:3 ratio of total DNA to PEI per well of a 6-well plate. The culture medium was replaced after 6 hours with mTesR+ (for iPSC transductions) or neurobasal media (for neuronal

639 transductions). The supernatant was collected after 48h and passed through a 0.45 µM polyether sulfone filter to remove
640 any cell debris. Large batches of virus were made together and small aliquots were stored at -80°C, to be thawed only once.

641 iPSCs were transduced with lentivirus containing guides against *MAPT* or NTC followed by puromycin selection (1 µg/mL)
642 48 hours-post transduction for 72 hours (until control, non-transduced cells were 100% dead) to generate tau^{KD} iPSCs.

643 iPSC-derived tau^{KD} neural progenitors were transduced with lentivirus containing tau constructs at 72 hours post-
644 differentiation using the doxycycline-induced Ngn2 cassette. Neural progenitors were lifted with StemPro Accutase Cell
645 Dissociation Reagent (5 min, 37C), pelleted and resuspended in neuronal differentiation media. Neural progenitors were
646 plated at $0.5x10^6$ cells in a single well of a 6-well plate. Lentiviruses containing either FUW-0N3R^{myc}, FUW-0N4R^{myc} or FUW-
647 0N3R^{EGFP} were added to the media upon re-plating. We did not observe any silencing of exogenously expressed tau in
648 differentiated neurons using the UbC promoter.

649 ***iPSC culture and neuronal differentiation***

650 Human iPSC cultures and neuronal differentiation protocols were performed as previously described with minor
651 modifications[60]. CRISPRi-iPSCs expressing inducible Ngn2 from AAVS1 safe harbor locus were maintained in mTesR1+
652 media with mTesR1+ supplements. iPSCs were plated on hESC Matrigel and maintained in mTesR1+ media (Stem Cell
653 Technologies). iPSCs were differentiated to glutamatergic neurons following established protocols[60]. iPSCs were lifted and
654 singularized using StemPro Accutase (5 min, 37C) followed by neutralization with mTesR1+ media. Cells were gently
655 pelleted for 5 minutes at 300*g*, then resuspended to $0.7x10^6$ cells/mL in neuronal induction media: KnockOut DMEM/F-12
656 (Gibco# 12660012) + 1x NEAA (Gibco#11140050) + 1x GlutaMAX (Gibco# 35050-061) + 10 nM Y27632 ROCK inhibitor
657 (Tocris# 125410) + 1x N2 max (Gibco #17502-048) + 2 µg/mL doxycycline hydrochloride (Sigma# D9891). A complete media
658 change was made the following day using the same media. The next day, another complete media change was made but
659 without ROCK inhibitor. Neural progenitors were lifted and dissociated with StemPro Accutase 72-hours post neuronal
660 induction, pelleted (5 min, 300*g*), and re-plated at $0.5x10^6$ cells per well of a 6-well plate that was first coated overnight with
661 poly-L-ornithine hydrobromide (0.1 mg/mL in borate buffer pH 8.5; Sigma, #P3655). The replating maturation media
662 contained: Neurobasal-A (Gibco# 10888-022) + 1x NEAA + 1xGlutaMAX + 10 nM Y27632 ROCK inhibitor + 2 µg/mL
663 doxycycline hydrochloride + 1x B-27 plus (Gibco# A3582801) + 10 ng/mL BDNF (PeproTech #450-02) + 10 ng/mL NT-3
664 (PeproTech #450-03) + 1 µg/mL laminin (Gibco# 23017-015). 50% media changes were made every 7 days with the same
665 media lacking ROCK inhibitor and doxycycline. iNeurons were harvested at the time points indicated within each figure and
666 figure legend.

667 ***Immunoprecipitation of phospho-tau***

668 Tau^{KD} iNeurons were re-plated at $2x10^7$ cells/plate on a PLO-coated 15-cm dish and transduced with FUW-0N3R^{EGFP}. At 32
669 days post-induction, iNeurons were washed twice with room temperature PBS and then harvested in the dish in 8 mL of
670 ice-cold RIPA buffer (supplemented with 2x protease inhibitors and 2x phosphatase inhibitors). The cells were transferred
671 to a conical tube and rotated at 4C for 10 minutes, followed by pelleting of debris by centrifugation at 17,000*g* for 10 min at
672 4C. The supernatant was collected and divided into 8 equal tubes (1 mL each, ~$2.5x10^6$ cells per tube) for phospho-tau
673 immunoprecipitation. 50 µL of lysate was collected from each tube and was supplemented with 50 µL of 4x Laemmli buffer
674 (supplemented with 100 mM DTT, and boiled for 15 min at 95C before SDS-PAGE) for the input lanes. Phospho-tau
675 antibodies were added to the remaining lysates and rotated at 4C overnight: pT181 mouse monoclonal (10µg), AT8 mouse
676 monoclonal (10µg), pT212 rabbit polyclonal (10µg), pT217 rabbit polyclonal (10µg), pT231 mouse monoclonal (10µg),
677 pS235 mouse monoclonal (15µg), pS396 rabbit polyclonal (5µg) or non-specific mouse or rabbit IgG (for IgG control). The
678 following morning, either Protein A (Neta/Sigma, GE28-9513-78) or Protein G (Neta/Sigma, GE28-9513-79) magnetic

679 sepharose beads were washed 3x with ice-cold RIPA buffer and incubated with each immunoprecipitation for 2 hours,
680 rotating at 4C. The beads were then gently pelleted and washed 3x with ice-cold RIPA buffer using a DynaMag-2 Magnet
681 rack (Fisher, 12-321-D). Affinity captured proteins were eluted into 170 µL of 2x Laemmli buffer (supplemented with 50 mM
682 DTT) at 95C for 15 minutes. Samples were subject to SDS-PAGE followed by co-blotting for phospho-tau epitopes.

683 ***Calculation of phospho-tau abundance and co-occurrence***

684 Affinity-captured phospho-tau was assumed to be monomeric and soluble due to the presence of deoxycholate, triton-X
685 and SDS in the lysis and wash buffers, and therefore co-blotted phospho-tau was assumed to be covalently-modified tau
686 rather than the result of tau multimerization. Volumes per well for each measurement for SDS-PAGE: input (5µL,
687 representative of ~6.25×10^3 cells, or 2.24% of the IP lane), IgG control or eluted phospho-tau (20µL, representative of
688 ~2.79×10^5 cells). Signal intensities in the input lane were back-calculated to 100% of the IP lane (by multiplication by 44.7.

689 *To calculate phospho-tau abundance*

690 The efficiency of phospho-tau that was affinity-captured by each phospho-specific antibody was calculated using
691 immunoblot:

692 A. Efficiency of phospho-tau capture = Intensity of p-tau IP lane / Back-calculated intensity of p-tau input lane.

693 Next, the percentage of total tau that was recovered within each affinity capture was calculated. This number represents
694 the percentage of phospho-tau that was recovered from the total tau lysate.

695 B. Efficiency of total tau capture = Intensity of total tau IP lane / Back-calculated intensity of total tau input lane.

696 Lastly, phospho-tau abundance was estimated by using a ratio of 'B / A'. In other words, of the A% of phospho-tau that was
697 recovered, B% of it was positive for the given phospho-tau epitope. For example, for a given replicate, if 2.57% of pT181
698 was recovered ('A'), and this was equal to 1.03% of total tau recovery ('B'), then 'B / A' = 1.03% / 2.57% = 39.9% of total tau
699 is phosphorylated at T181. Abundance was calculated using the average of a technical repeat for each replicate, and then
700 averaged across all replicates: pT181 (n=4), AT8 (n=5), pT212 (n=4), pT217 (n=6), pT231 (n=6), pS235 (n=6), pS396 (n=4).

701 *To calculate phospho-tau co-occurrence*

702 The same logic as above was used to calculate phospho-tau co-occurrence:

703 C. Efficiency of phospho-tau co-occurrence = Intensity of p-tau co-blot in IP lane / Back-calculated intensity of co-
704 blotted p-tau in input lane.

705 Co-occurrence was calculated using a ratio of 'C / A'. In other words, of the A% of phospho-tau that was recovered, C% of
706 it was positive for the given co-occurring phospho-tau epitope. For example, for a given replicate if 0.052% of AT8 was
707 recovered ('C') from the pT181 immunoprecipitation (A = 2.57%), then 'C / A' = 0.052% / 2.57% = 20.1% of pT181 molecules
708 carry a phospho-modification at the AT8 epitope.

709 Recovery of tau phosphorylated at Ser235 was too inefficient to reliably quantify co-occurrence of phosphorylation;
710 therefore, these calculations were omitted.

711 Combinations of three co-occurring phospho-epitopes were predicted by minimum linkage analysis, which ranks trios based
712 on their weakest link by accounting for co-occurrence in both directions. In other words, low P(A, B) will penalize the score
713 even if P(A, C) + P (B, C) is high.

714 ***Top-down mass spectrometry***

715 Top-down mass spectrometry (TD-MS) of tau proteoforms was performed essentially as previously described[61]. The
716 harvested iNeurons (8 million cells, DPI 30) were suspended in 500 µL of homogenization buffer composed of Ham's F12

717 medium supplemented with 1× Halt Protease and Phosphatase Inhibitor, 5 mM EDTA, and 0.45% CHAPS, and left in 4 °C
718 for half an hour for cell lysis. Afterwards, the cell lysate was subjected to sonication on ice for 20 seconds at 40% power,
719 using a pulse cycle of 2 seconds on and 3 seconds off. The lysate was then centrifuged at 17,000*g* for 30 minutes at 4°C
720 to separate cell debris, and supernatants were collected for tau IP. Tau antibody-conjugated beads were prepared by
721 incubating 10 µg each of HT-7 and Tau-5 antibodies with 50 µL of Protein A/G beads at room temperature for 10 minutes.
722 The prepared conjugated beads were added to 500 µL of the cell lysate and incubated overnight at 4°C with end-to-end
723 rotation. Afterwards, the beads were subjected to a series of wash steps: twice with 500 µL homogenization buffer, twice
724 with a 1:1 mixture of homogenization buffer and water, and three times with 500 µL of water. Finally, the tau proteins were
725 eluted from the beads incubation in 150 µL of 10% formic acid at room temperature for 30 minutes. The eluates were flash-
726 frozen and stored at -80 °C for further analysis.

727 Individual ion mass spectrometry (I^2MS) is an advanced top-down MS technique that enables direct mass readout of
728 complex tau proteoforms at the intact level[62]. The SampleStream platform (Integrated Protein Technologies) was interfaced
729 with a Q Exactive HF mass spectrometer (Thermo Fisher Scientific) using the Ion Max source equipped with a HESI II probe
730 to provide online buffer exchange and I^2MS analysis. Triplicate I^2MS runs were performed for the iNeuron-derived tau IP
731 sample. For each run, 50 µL of immunoprecipitated tau samples were cleaned and buffer-exchanged into a solution of 0.2%
732 (v/v) formic acid and 30% (v/v) acetonitrile in water, followed by direct injection into the mass spectrometer at a flow rate of
733 1.6 µL/min for I^2MS analysis. On the mass spectrometer, automated Ion Control (AIC) was utilized to dynamically adjust the
734 injection time based on ion signal density, ensuring optimal detection of individual ion signals. Additional mass spectrometry
735 settings included an Orbitrap central electrode voltage of 1 kV, trapping gas pressure of 0.3, m/z range of 650-2,500, a
736 resolution of 120,000 at m/z 200 (corresponding to a 1 s transient time), a spray voltage of 3.1 kV, in-source CID energy of
737 15 eV, and a source temperature of 320 °C. I^2MS data were acquired over a 50-minute period per run, totaling approximately
738 3,000 scans.

739 All the I^2MS transient files were converted to .storx files and processed using STORIboard
740 (https://www.proteinaceous.net/storiboard) with the voting charge assignment algorithm. After processing, .mzML files were
741 generated, presenting the mass domain spectrum of each run. The mass spectra were annotated by TDValidator
742 (Proteinaceous, https://www.proteinaceous.net/tdvalidator). Tau 0N3R proteoforms were matched to spectral peaks based
743 on intact mass, using a mass accuracy window of ±50 parts per million (ppm) and a mass tolerance of 1.8 Da. The 0N3R
744 proteoforms were quantified by their relative abundance.

745 ***Intact microtubule fractionation from iNeurons***

746 Intact microtubules were fractionated from soluble cytosolic proteins using tau^{KD} iNeurons expressing either FUW-0N3R^{myc}
747 or FUW-0N4R^{myc} at 12 days post-neuronal induction following established protocols[63]. Neurons were plated at $0.5x10^6$ cells
748 in a single well of a 12-well PLO-coated plate.

749 Fresh microtubule stabilization buffer (MSB) was made containing 100 mM PIPES (Millipore Sigma #P1851) + 1 mM $MgSO_4$
750 (M2643) + 2 mM EGTA (E3889) + 0.1 mM EDTA (E8008) + 2 M glycerol (G9012). The pH was adjusted to 6.75 with KOH
751 (221473) to fully dissolve the PIPES. 1 mM PMSF (10837091001) + 1x protease inhibitor (P8340) + 1x Halt phosphatase
752 inhibitor cocktail (78420) were added fresh immediately before the assay. MSB was pre-warmed to 37C.

753 The media was aspirated, and the cells were gently washed once with MSB. Next, the cells were incubated with 300 µL of
754 pre-warmed MSB containing 1% Tx-100 for 5 min at 37C. The plate was gently tilted after the addition of the buffer. After 5
755 minutes, the buffer was collected (and placed on ice) and the cells were washed with 300 µL of the same buffer and
756 combined with the initial collection, termed the cytosolic fraction. Cells with intact cytoskeletons remained adhered to the

757 well. These were scraped in 600 µL MSB containing 1% Tx-100 and placed on ice (intact MT fraction). Following the
758 extractions, the two fractions were brought to equivalent volumes in MSB + 1% Tx-100. 200 µL 4X Laemmli SDS loading
759 buffer (supplemented with 10 mM DTT) was added to each sample. Samples were boiled for 20 min at 95C and immediately
760 subject to separation by SDS-PAGE for immunoblot.

761 The same protocol was used for immunofluorescence except cells were either incubated for 5 min at 37C in MSB (no
762 cytosolic extraction) or MSB + 1% Tx-100 (cytosolic extraction), followed by a single wash in the same buffer and then
763 fixation by 4% PFA in PBS for 20 min at room temperature.

764 Anti-detyrosinated α-tubulin was used as a marker for intact MTs, and anti-NSE was used as a cytosolic/membrane marker.

765 ***Immunofluorescence in primary mouse neurons and iNeurons***

766 Immunofluorescence was performed essentially as previously described[59]. Cells were plated and maintained on tissue-
767 culture treated and coated glass coverslips (poly-L-laminin for primary neurons, poly-L-ornithine for iNeurons). Cells were
768 washed twice with PBS + 1 mM $MgCl_2$ and fixed in 4% paraformaldehyde (PFA) for 20 min at room temperature. The PFA
769 was washed out twice with PBS + 1 mM $MgCl_2$, then the cells were permeabilized for 5 minutes with 0.1% Tx-100 in PBS-
770 T, followed by incubation with blocking buffer (PBS-T + 5% BSA) for 1 hour at room temperature. Cells were incubated
771 overnight at 4C in primary antibody: β-tubulin III rabbit polyclonal (1:500), β-tubulin III mouse monoclonal (1:500), α-tubulin
772 1a mouse monoclonal (1:500), detyrosinated α-tubulin rabbit polyclonal (1:500).

773 ***Pharmacological reagents***

774 The following pharmacological reagents were utilized throughout this study: Nocodazole (10 µM final; 12-281-0),
775 demecolcine (1 µM final; D7385; lot #102753904), paclitaxel (10 µM final; T1912; lot #1003615845), latrunculin A (2 µM
776 final; L5163; lot #0000373456), LB-100 (20 µM final; 29105; lot #0613520-17), Calyculin A (20 nM final; C5552; lot
777 #0000366393), AKT1 inhibitor VIII (20 µM final; 14870; lot #0613313-34), Erk1/2 inhibitor I (10 nM final; A1176841; lot
778 #HA2), GSK3β BIO-1 inhibitor (5 µM final; 13123; lot #0586619-49).

779 ***Cytoskeleton manipulation by pharmacological reagents***

780 iNeurons (*DPI 21*) were treated with either DMSO, nocodazole (10 µM), demecolcine (1 µM), paclitaxel (10 µM) or latrunculin
781 A (2 µM) for 90 minutes in complete neuronal media. Cells were washed twice with PBS at room temperature and harvested
782 for Western blot in ice-cold RIPA buffer supplemented with protease and phosphatase inhibitors.

783 ***Pharmacological microtubule catastrophe by nocodazole treatment***

784 Nocodazole was resuspended in DMSO to 10 mM, aliquoted and stored at -20C. DPI 25 iNeurons ($0.5x10^6$ per well of a 6-
785 well plate for immunoblot, $0.4x10^5$ per well of a 24-well plate for immunofluorescence) were washed once with ice-cold PBS
786 for 5 min to facilitate MT catastrophe, and then treated with 10 µM nocodazole (final) in pre-warmed complete neuronal
787 media for either 15 minutes or 90 minutes at 37C. For MT recovery experiments, nocodazole was washed out by aspirating
788 out the media and performing three washes with pre-warmed neuronal media without nocodazole. After the third wash was
789 removed, the cells were incubated at 37C in complete neuronal media without nocodazole for either 1 hour, 3 hours or 6
790 hours to allow for MT recovery. At the final time point, for immunoblot, the cells were washed twice with room temperature
791 PBS then lysed and scraped in ice-cold RIPA buffer supplemented with protease inhibitors and phosphatase inhibitors on
792 ice. Following 10 min of rotation at 4C, debris were pelleted at 17,000*g* for 10 min at 4C, the supernatant was collected and
793 supplemented with 4x Laemmli buffer + 10 mM DTT, boiled for 20 min at 95C, then subject to SDS-PAGE followed by
794 immunoblot. For immunofluorescence, the cells were washed twice with 0.1M PHEM buffer (pH 7.2) at room temperature
795 and fixed for 15 min in 4%PFA/0.25%GA in 0.1M PHEM buffer (pH 7.2) at room temperature. The fixative was washed out

796 3x with PHEM buffer, and immunofluorescence was performed as described above except PBS was replaced with PHEM
797 buffer for all steps including washing and blocking buffer (5% BSA in PHEM-T). Stable microtubules were detected by anti-
798 acetylated α-tubulin and anti-detyrosinated α-tubulin antibodies.

799 ***Kinase/phosphatase inhibition***

800 iNeurons (*DPI 30*) were treated for 90 minutes with nocodazole (10 μM) and either LB-100 (20 μM) or Calyculin A (20 nM).
801 Cells were either washed and collected for Western blot at this point, or the nocodazole and phosphatase inhibitors were
802 washed out 3x with pre-warmed complete media (lacking nocodazole and phosphatase inhibitors) and allowed to recover
803 at 37C for 3 hours prior to harvesting. For kinase inhibition, neurons were treated for 90 minutes with 10 μM nocodazole
804 followed by 3x washout, followed by incubation with AKT1 inhibitor VIII (20 μM) for 3 hours at 37C. At this final timepoint,
805 cells were then harvested, as described above, for Western blot.

806 ***SDS-PAGE and quantitative immunoblotting***

807 Proteins were separated by SDS-PAGE for immunoblotting as previously described[59]. Briefly, 8-15% Laemmli gels (10.3%T
808 and 3.3%C) were used to separate proteins on Bio-Rad apparati. 2.5 mM final DTT was used in SDS Laemmli buffer unless
809 indicated otherwise. Proteins were transferred onto nitrocellulose (pore-size = 0.45 μm; GE Healthcare) and blocked with
810 Every Blot Blocking Buffer (Bio-Rad). Immunoblotting was performed by incubating the blocked membranes with primary
811 antibodies in blocking buffer for overnight incubation. Following 5 washes with TBS-Tween 20 (0.1%), blots were incubated
812 with secondary antibodies (goat anti-rabbit conjugated to IRDye 680RD or 800CW; LI-COR) at 1/10,000 in blocking buffer
813 for 1-2 hours. Immunoblots were washed 5x with TBS-T and dried, then scanned on an Odyssey CLx (LI-COR) and
814 quantified using Image-Studio software (LI-COR).

815 ***Purification of recombinant tau wildtype and phospho-mimic proteins***

816 Recombinant tau proteins were expressed in BL21(DE3) cells and purified as previously described with minor
817 modifications[16]. *MAPT* was cloned into the pET-HT vector with a N-terminal 6xHis-TEV fusion, and transformed into
818 BL21(DE3) competent cells. Overnight starter cultures were incubated in 500 mL LB broth at 37C until OD600=0.6, at which
819 time protein expression was induced with 1 mM isopropyl-β-D-1-thiogalactopyranoside (IPTG) at 18C for 16 hours. Bacteria
820 were then pelleted (4000*g* for 20 min at 4C) and resuspended in cold lysis buffer (20 mM Tris pH 8.0, 150 mM NaCl, 1
821 Roche EDTA-free protease inhibitor tablet, 1 mg/mL lysozyme, 20 mM imidazole, 1 mM PMSF, 1x DNase, 1 mM $MgCl_2$).
822 Cells were rotated at 4C for 30 minutes followed by sonication on ice (2 minutes; 1 sec on, 2 sec off) and centrifuged again
823 (20,000*g*, 30 minutes at 4C) to remove cellular debris. The supernatant was subject to affinity capture using Ni-NTA resin
824 (Fisher; PI88222) for 1 hour, rotating, at 4C. Unbound proteins were washed away with 6 column volumes of buffer
825 containing 20 mM Tris pH 8.0 + 150 mM NaCl + 20 mM imidazole, then eluted in the same buffer containing 300 mM
826 imidazole. The eluted 6xHis-TEV-tau protein was buffer exchanged to the previous buffer (20 mM Tris pH 8.0 + 150 mM
827 NaCl + 20 mM imidazole) using a 10 kDa MWCO Amicon Ultra-15 Centrifugal Filter Unit (Millipore #UFC9010), concentrated
828 to ~1.5 mL, and incubated with super TEV protease-6xHis (1:300 enzyme to tau molar ratio) and 1 mM DTT, rotating at 4C
829 overnight. The following day, the mixture was diluted 15-fold in 20 mM Tris pH 8.0 + 150 mM NaCl + 20 mM imidazole to
830 dilute the DTT and reverse-Ni NTA affinity capture (1 hour, rotating at 4C) was used to remove the TEV-6xHis protease from
831 the mixture. The flowthrough (containing tau) was collected and buffer exchanged into 20 mM Tris pH 8.0 + 150 mM NaCl
832 + 1 mM EDTA + 1 mM TCEP, concentrated to ~2 mL and injected onto a HiLoad 16/600 Superdex 200 PG column for size
833 exclusion in the same buffer. Fractions containing tau were identified by UV-absorption at 280 nm. Fractions containing
834 >95% pure tau were pooled, concentrated to ~100 μM (determined by NanoDrop), aliquoted, flash frozen in liquid N_2 and
835 stored at -80C to be used for a single freeze-thaw cycle.

836 Tau phospho-mimic mutation sequences are as follows: Thr181Glu (ACA>GAA): Thr217Glu (ACC>GAA): Thr231Glu
837 (ACT>GAA): Ser235Glu (TCG>GAG): Ser262Glu (TCC>GAA): Ser396Glu (TCG>GAG): Ser404Glu (TCT>GAA).

838 ***Purification of tubulin from bovine brains***

839 Tubulin was purified from fresh bovine brains as previously described[64] and flash frozen in BRB80 buffer (80 mM PIPES +
840 1 mM $MgCl_2$ + 1 mM EGTA, pH 6.8). Frozen aliquots were thawed on ice and clarified by centrifugation at 100,000*g* for 6
841 min at 4C. The supernatant was collected, and the concentration of tubulin was estimated using NanoDrop. Clarified
842 samples were used immediately for the MT polymerization assay, and fresh aliquots were clarified for each replicate.

843 ***Microtubule polymerization assay by turbidity***

844 Polymerization of tubulin was monitored by light scatter at 340 nm as previously described with minor adjustments[15]. Freshly
845 clarified tubulin (20 μM final) was incubated with tau protein (10 μM final) in cold BRB80 buffer supplemented with fresh 1
846 mM DTT. A 250 μL reaction was made on ice and 100x fresh GTP (1 mM final) was added and mixed by pipette trituration
847 on ice. After 5 minutes, 200 μL were quickly transferred to a pre-warmed 96-well black-walled clear bottom plate and the
848 reaction was monitored at 37C for 45 minutes on a M1000 Tecan spectrophotometer. 9 flash measurements were made
849 and averaged per well per timepoint throughout the kinetic measurement. Each replicate of 0N3R tau wildtype and phospho-
850 mimics were measured in parallel, and similarly so for 0N4R. Three independent measurements were made and compared
851 to their respective wildtype measurements for each sample, to account for read-to-read variability. Afterwards samples were
852 returned to ice for 5 min to confirm that the samples could be depolymerized (thus eliminating concern for potential protein
853 aggregation). Polymerization curves were corrected by subtracting a plate blank, a buffer blank and a tubulin + GTP (no
854 tau) measurement from each sample. Curves were then normalized to the maximum data point for each sample. The time
855 to 50% V_{max} was compared to wildtype for each isoform and averaged for final measurements.

856 ***Triton-X solubility assay of PS19 transgenic mouse brains***

857 Mouse brains from PS19 mice were dissected on ice at either post-natal day 0 or at 9-months. Brain lysates were subject
858 to Triton-X (Tx) solubility as previously described[65]. Briefly, brains were rinsed twice with ice cold PBS, then homogenized
859 in 0.1% Tx-100 in PBS supplemented with protease and phosphatase inhibitors. Samples were rotated for 30 min at 4C
860 and then sonicated 10x at 10% power (0.5 sec on, 1 sec off). The tissue was then centrifuged at 17,000*g* for 90 min at 4C.
861 The supernatant (soluble fraction) was collected, and the pellet (insoluble fraction) was resuspended in an equal volume of
862 lysis buffer as the supernatant. Each sample volume was doubled using 4x Laemmli buffer (supplemented with 10 mM DTT)
863 and sonicated again: 20x at 10% power (0.5 sec on, 1 sec off). The samples were then boiled at 95C for 20 min before
864 loading equal volumes of each fraction on SDS-PAGE, followed by immunoblot for tau. Approximately two-fold more tissue
865 levels were loaded for 9-month-old samples compared to neonates (as indicated by β-actin immunoblot) to improve
866 detection of lowly-detected phosphorylation epitopes, particularly at sites pS202/pT205, pT231 and pS262. Insoluble tau
867 was calculated as a percentage of total protein per sample and/or normalized to β-actin, as indicated.

868 ***Antibody list***

Antibody	Host Species	Manufacturer	Catalog #	Working Dilution
Tau5 (pan-tau)	Mouse	Invitrogen	MA5-12808	1:1000 (WB)
Tau5 (pan-tau)	Rabbit	Novus	NB015844	1:1000 (WB)
HT7 (pan-tau)	Mouse	Invitrogen	MN1000	For IP only
AT270 (Tau pT181)	Mouse	Invitrogen	MN1050	1:1000 (WB)
AT8 (Tau pS202/pT205)	Mouse	Invitrogen	MN1020	1:1000 (WB) 1:100 (ICC)
Tau pT212	Rabbit	Invitrogen	44740G	1:1000 (WB)
Tau pS214	Rabbit	Invitrogen	44742G	1:500 (WB)

AT100 (Tau pT212/pS214)	Mouse	Invitrogen	MN1060	1:1000 (WB)
Tau pT217	Rabbit	Invitrogen	44-744	1:1000 (WB)
AT180 (Tau pT231)	Mouse	Invitrogen	MN1040	1:1000 (WB) 1:100 (ICC)
Tau pS235	Mouse	Millipore Sigma	MABN2275	1:500 (WB)
Tau pS262	Rabbit	Invitrogen	44-750G	1:500 (WB)
Tau pS396	Rabbit	Invitrogen	44-752G	1:1000 (WB)
Tau pS404	Rabbit	Invitrogen	44-758G	1:1000 (WB) 1:100 (ICC)
Tau pS416	Rabbit	Invitrogen	PA1-4719	1:1000 (WB) 1:100 (ICC)
Tau pS422	Rabbit	Invitrogen	44-764G	1:1000 (WB)
NeuN	Rabbit	Invitrogen	PA5-74899	1:1000 (WB)
GAPDH	Rabbit			1:1000 (WB)
Tau 3R	Mouse	Millipore Sigma	05803MI	1:1000 (WB)
β-tubulin III	Mouse	R&D Systems	MAB1195	1:1000 (WB) 1:250 (ICC)
β-tubulin III	Rabbit	Invitrogen	PA5-86069	1:250 (ICC)
α-tubulin 1A	Rabbit	Abcam	ab18251	1:1000 (WB)
Detyrosinated α-tubulin	Rabbit	Millipore Sigma	AB3201	1:1000 (WB) 1:250 (ICC)
Acetylated α-tubulin (aK40)	Mouse	Invitrogen	6-11B-1	1:1000 (WB)
β-actin	Mouse	Invitrogen	MA1-744	1:1000 (WB)
Hsp70	Mouse	Invitrogen	MA3-007	1:250 (WB)
NSE	Rabbit	Abcam	ab53025	1:1000 (WB)
MAP1A	Rabbit	Invitrogen	PA558642	1:1000 (WB)
MAP1B	Rabbit	Invitrogen	PA578052	1:1000 (WB)
MAP2	Rabbit	Millipore Sigma	AB5622	1:1000 (WB)
SV2a	Rabbit	Thermo Fisher	PA5-115990	1:1000 (WB)
pAkt1 (pS473)	Rabbit	Invitrogen	44621G	1:500 (WB)
Akt1	Mouse	Invitrogen	AHO1112	1:250 (WB)
pErk1/2 (pT202/pT204)	Mouse	Invitrogen	501128621	1:1000 (WB)
Erk1/2	Rabbit	Invitrogen	MA515134	1:1000 (WB)
pGSK3β (pY216)	Rabbit	Invitrogen	44604G	1:1000 (WB)
GSK3β	Mouse	Invitrogen	MA515597	1:1000 (WB)
Methyl-PP2a (mL309)	Mouse	Santa Cruz	sc-81603 (2A10)	1:200 (WB)
pPP2a (pY307)	Rabbit	Invitrogen	PIPA536874	1:500 (WB)
PP2a	Rabbit	Invitrogen	PA517510	1:1000 (WB)
VDAC1	Mouse	Millipore Sigma	MABN504	1:2000 (WB)

All anti-tau antibodies were knockout/knockdown validated using either mouse brains, iPSC-derived neurons or both. Anti-pS422 had a strong, non-specific band at ~50 kDa, slightly beneath a faint p-tau band, in iPSC-derived neurons but not in mouse brains. The non-specific signal occluded reliable quantification in iNeurons. AT100 (pT212/pS214) was not detected in iNeurons, and in concurrence anti-pS214 (Invitrogen, #44742G) was inconsistently detected as a very faint band that could not be reliably quantified.

Statistical analysis

All experiments were performed using reagents that were aliquoted to minimize freeze-thaw cycles and improve reproducibility. Each 'n' was collected independently, as indicated in the figure legends. SC randomized and blinded NNN to sample identifies (lentivirus identities, mouse ages, sample treatments) for data analysis. All analyses were performed using PyCharm Community Edition 2023.2.4. Statistical significance for comparisons between two sample groups was determined by two-tailed Student's *t* test. Significance for curve comparisons for nocodazole-treated sample groups was

determined by post-hoc Tukey's HSD test. Significance for curve comparisons for MT polymerization reactions was determined by two-way ANOVA analysis.

ACKNOWLEDGEMENTS

This work was supported by funding to N.N.N. (F31NS098623, F32AG079537, K99AG084855, AARF-22-924146), to E.R. (RF1AG053951), to O.S. (DP2-GM137416, Target ALS, Chan-Zuckerberg Institute), to M.S. (R01AG083949, R01NS095988, R01AG052505) and to N.L.K. (P30CA060553 and P41GM108569).

AUTHOR INFORMATION

AUTHORS AND AFFILIATIONS

Department of Chemistry, University of Pennsylvania, Philadelphia, PA, USA

Nima N Naseri, Elizabeth Rhoades

Center for Cellular and Molecular Therapeutics, Children's Hospital of Philadelphia, Philadelphia, PA, USA

Nima N Naseri, Sapanna Chantarawong, Ophir Shalem

Department of Chemistry, Northwestern University, Evanston, Illinois 60208, United States

Tian Xu, Steven M Patrie, Neil L Kelleher

Appel Institute for Alzheimer's Research, and Feil Family Brain & Mind Research Institute, Weill Cornell Medicine, New York, NY, USA

Manu Sharma

Department of Genetics, Perelman School of Medicine, University of Pennsylvania, Philadelphia, PA, USA

Ophir Shalem

Department of Biochemistry & Biophysics, Perelman School of Medicine, University of Pennsylvania, Philadelphia, PA, USA

Elizabeth Rhoades

CONTRIBUTIONS

NNN and ER conceived the project, directed by ER and OS. All experiments were performed and analyzed by NNN except for top-down mass spectrometry, performed by TX under guidance by SMP and NLK. SC provided technical support. MS provided mice for this study.

CORRESPONDING AUTHOR

Correspondence to Elizabeth Rhoades.

ETHICS DECLARATIONS

The authors declare no competing interests.

DATA AVAILABILITY

The raw immunoblots generated in this study are available in the supporting information.

REFERENCES

1 Brion, J., Passareiro, H., Nunez, J. & Flament-Durand, J. Mise en evidence immunologique de la proteine tau au niveau des lesions de degenerescence neurofibril-laire de la maladie d'Alzheimer. *Arch Biol (Bruxelles)* **95**, 229-235 (1985).

2 Grundke-Iqbal, I. *et al.* Abnormal phosphorylation of the microtubule-associated protein tau (tau) in Alzheimer cytoskeletal pathology. *Proc Natl Acad Sci U S A* **83**, 4913-4917 (1986).

3 Ihara, Y., Nukina, N., Miura, R. & Ogawara, M. Phosphorylated tau protein is integrated into paired helical filaments in Alzheimer's disease. *The Journal of Biochemistry* **99**, 1807-1810 (1986).

4 Lövestam, S. *et al.* (eLife Sciences Publications, Ltd, 2025).

5 Thijssen, E. H. *et al.* Plasma phosphorylated tau 217 and phosphorylated tau 181 as biomarkers in Alzheimer's disease and frontotemporal lobar degeneration: a retrospective diagnostic performance study. *Lancet Neurol* **20**, 739-752 (2021). https://doi.org:10.1016/s1474-4422(21)00214-3

6 Janelidze, S. *et al.* Plasma P-tau181 in Alzheimer's disease: relationship to other biomarkers, differential diagnosis, neuropathology and longitudinal progression to Alzheimer's dementia. *Nature medicine* **26**, 379-386 (2020). https://doi.org:10.1038/s41591-020-0755-1

7 Brickman, A. M. *et al.* Plasma p-tau181, p-tau217, and other blood-based Alzheimer's disease biomarkers in a multi-ethnic, community study. *Alzheimers Dement* **17**, 1353-1364 (2021). https://doi.org:10.1002/alz.12301

8 Palmqvist, S. *et al.* Blood Biomarkers to Detect Alzheimer Disease in Primary Care and Secondary Care. *JAMA* **332**, 1245-1257 (2024). https://doi.org:10.1001/jama.2024.13855

9 Pope, W. *et al.* Phosphorylated tau epitope of Alzheimer's disease is coupled to axon development in the avian central nervous system. *Experimental neurology* **120**, 106-113 (1993).

10 Yu, Y. *et al.* Developmental regulation of tau phosphorylation, tau kinases, and tau phosphatases. *Journal of Neurochemistry* **108**, 1480-1494 (2009). https://doi.org:10.1111/j.1471-4159.2009.05882.x

11 Hefti, M. M. *et al.* Tau phosphorylation and aggregation in the developing human brain. *Journal of Neuropathology & Experimental Neurology* **78**, 930-938 (2019).

12 Kenessey, A. & Yen, S. H. The extent of phosphorylation of fetal tau is comparable to that of PHF-tau from Alzheimer paired helical filaments. *Brain Res* **629**, 40-46 (1993). https://doi.org:10.1016/0006-8993(93)90478-6

13 Andreadis, A. Tau gene alternative splicing: expression patterns, regulation and modulation of function in normal brain and neurodegenerative diseases. *Biochimica et biophysica acta* **1739**, 91-103 (2005). https://doi.org:10.1016/j.bbadis.2004.08.010

14 Wesseling, H. *et al.* Tau PTM Profiles Identify Patient Heterogeneity and Stages of Alzheimer's Disease. *Cell* **183**, 1699-1713.e1613 (2020). https://doi.org:10.1016/j.cell.2020.10.029

15 McKibben, K. M. & Rhoades, E. Independent tubulin binding and polymerization by the proline-rich region of Tau is regulated by Tau's N-terminal domain. *The Journal of biological chemistry* **294**, 19381-19394 (2019). https://doi.org:10.1074/jbc.RA119.010172

16 Acosta, K. *et al.* Structural insights into the role of the proline rich region in tau function. *Structure* (2025).

17 Sengupta, A. *et al.* Phosphorylation of tau at both Thr 231 and Ser 262 is required for maximal inhibition of its binding to microtubules. *Arch Biochem Biophys* **357**, 299-309 (1998). https://doi.org:10.1006/abbi.1998.0813

18 Goode, B. L. *et al.* Functional interactions between the proline-rich and repeat regions of tau enhance microtubule binding and assembly. *Molecular biology of the cell* **8**, 353-365 (1997).
19 Preuss, U., Biernat, J., Mandelkow, E.-M. & Mandelkow, E. The 'jaws' model of tau-microtubule interaction examined in CHO cells. *Journal of cell science* **110**, 789-800 (1997).
20 Brotzakis, Z. F. *et al.* A structural ensemble of a tau-microtubule complex reveals regulatory tau phosphorylation and acetylation mechanisms. *ACS Central Science* **7**, 1986-1995 (2021).
21 Kellogg, E. H. *et al.* Near-atomic model of microtubule-tau interactions. *Science (New York, N.Y.)* **360**, 1242-1246 (2018).
22 Schwalbe, M. *et al.* Structural Impact of Tau Phosphorylation at Threonine 231. *Structure* **23**, 1448-1458 (2015). https://doi.org:https://doi.org/10.1016/j.str.2015.06.002
23 Alonso, A. d. C. *et al.* Interaction of tau isoforms with Alzheimer's disease abnormally hyperphosphorylated tau and in VitroPhosphorylation into the disease-like protein. *Journal of Biological Chemistry* **276**, 37967-37973 (2001).
24 Drepper, F. *et al.* A combinatorial native MS and LC-MS/MS approach reveals high intrinsic phosphorylation of human Tau but minimal levels of other key modifications. *Journal of Biological Chemistry* **295**, 18213-18225 (2020).
25 Stefanoska, K. *et al.* Alzheimer's disease: Ablating single master site abolishes tau hyperphosphorylation. *Science advances* **8**, eabl8809 (2022).
26 Singh, T. J., Grundke-Iqbal, I. & Iqbal, K. Differential phosphorylation of human tau isoforms containing three repeats by several protein kinases. *Arch Biochem Biophys* **328**, 43-50 (1996). https://doi.org:10.1006/abbi.1996.0140
27 Cho, J.-H. & Johnson, G. V. W. Glycogen Synthase Kinase 3β Phosphorylates Tau at Both Primed and Unprimed Sites: DIFFERENTIAL IMPACT ON MICROTUBULE BINDING *. *Journal of Biological Chemistry* **278**, 187-193 (2003). https://doi.org:10.1074/jbc.M206236200
28 Li, T., Hawkes, C., Qureshi, H. Y., Kar, S. & Paudel, H. K. Cyclin-Dependent Protein Kinase 5 Primes Microtubule-Associated Protein Tau Site-Specifically for Glycogen Synthase Kinase 3β. *Biochemistry* **45**, 3134-3145 (2006). https://doi.org:10.1021/bi051635j
29 Islam, T. *et al.* Phospho-tau serine-262 and serine-356 as biomarkers of pre-tangle soluble tau assemblies in Alzheimer's disease. *Nature medicine*, 1-15 (2025).
30 Haj-Yahya, M. *et al.* Site-specific hyperphosphorylation inhibits, rather than promotes, tau fibrillization, seeding capacity, and its microtubule binding. *Angewandte Chemie International Edition* **59**, 4059-4067 (2020).
31 Augustinack, J. C., Schneider, A., Mandelkow, E. M. & Hyman, B. T. Specific tau phosphorylation sites correlate with severity of neuronal cytopathology in Alzheimer's disease. *Acta Neuropathol* **103**, 26-35 (2002). https://doi.org:10.1007/s004010100423
32 Schneider, A., Biernat, J., von Bergen, M., Mandelkow, E. & Mandelkow, E. M. Phosphorylation that Detaches Tau Protein from Microtubules (Ser262, Ser214) Also Protects It against Aggregation into Alzheimer Paired Helical Filaments. *Biochemistry* **38**, 3549-3558 (1999). https://doi.org:10.1021/bi981874p
33 Rajbanshi, B., Guruacharya, A., Mandell, J. W. & Bloom, G. S. Localization, induction, and cellular effects of tau phosphorylated at threonine 217 1. *Alzheimer's & Dementia* **19**, 2874-2887 (2023).
34 Gilley, J. *et al.* Mislocalization of neuronal tau in the absence of tangle pathology in phosphomutant tau knockin mice. *Neurobiology of aging* **39**, 1-18 (2016).
35 Ulrich, G. *et al.* Phosphorylation of nuclear Tau is modulated by distinct cellular pathways. *Scientific reports* **8**, 17702 (2018).
36 Li, D. & Cho, Y. K. High specificity of widely used phospho-tau antibodies validated using a quantitative whole-cell based assay. *Journal of Neurochemistry* **152**, 122-135 (2020). https://doi.org:https://doi.org/10.1111/jnc.14830
37 Ercan, E. *et al.* A validated antibody panel for the characterization of tau post-translational modifications. *Molecular neurodegeneration* **12**, 1-19 (2017).
38 Ellis, M. J. *et al.* Validation of Tau antibodies for use in western blotting and immunohistochemistry. *BioRxiv*, 2023.2004. 2013.536711 (2023).
39 Lapasset, L. *et al.* Rejuvenating senescent and centenarian human cells by reprogramming through the pluripotent state. *Genes & development* **25**, 2248-2253 (2011).
40 Patterson, M. *et al.* Defining the nature of human pluripotent stem cell progeny. *Cell research* **22**, 178-193 (2012).
41 Capano, L. S. *et al.* Recapitulation of endogenous 4R tau expression and formation of insoluble tau in directly reprogrammed human neurons. *Cell Stem Cell* **29**, 918-932. e918 (2022).

42 Bravo, C. P. *et al.* Human iPSC 4R tauopathy model uncovers modifiers of tau propagation. *Cell* **187**, 2446-2464. e2422 (2024).

43 Mazet, F. *et al.* A high-density immunoblotting methodology for quantification of total protein levels and phosphorylation modifications. *Sci Rep* **5**, 16995 (2015). https://doi.org:10.1038/srep16995

44 Zheng-Fischhöfer, Q. *et al.* Sequential phosphorylation of Tau by glycogen synthase kinase-3beta and protein kinase A at Thr212 and Ser214 generates the Alzheimer-specific epitope of antibody AT100 and requires a paired-helical-filament-like conformation. *Eur J Biochem* **252**, 542-552 (1998). https://doi.org:10.1046/j.1432-1327.1998.2520542.x

45 Goedert, M., Jakes, R. & Vanmechelen, E. Monoclonal antibody AT8 recognises tau protein phosphorylated at both serine 202 and threonine 205. *Neuroscience Letters* **189**, 167-170 (1995). https://doi.org:https://doi.org/10.1016/0304-3940(95)11484-E

46 Otvos, L., Jr. *et al.* Monoclonal antibody PHF-1 recognizes tau protein phosphorylated at serine residues 396 and 404. *J Neurosci Res* **39**, 669-673 (1994). https://doi.org:10.1002/jnr.490390607

47 Rye, D., Leverenz, J., Greenberg, S., Davies, P. & Saper, C. The distribution of Alz-50 immunoreactivity in the normal human brain. *Neuroscience* **56**, 109-127 (1993).

48 Dujardin, S. *et al.* Tau molecular diversity contributes to clinical heterogeneity in Alzheimer's disease. *Nature medicine* **26**, 1256-1263 (2020). https://doi.org:10.1038/s41591-020-0938-9

49 Mirbaha, H. *et al.* Seed-competent tau monomer initiates pathology in a tauopathy mouse model. *The Journal of biological chemistry* **298**, 102163 (2022). https://doi.org:10.1016/j.jbc.2022.102163

50 Hanger, D. P., Betts, J. C., Loviny, T. L. F., Blackstock, W. P. & Anderton, B. H. New Phosphorylation Sites Identified in Hyperphosphorylated Tau (Paired Helical Filament-Tau) from Alzheimer's Disease Brain Using Nanoelectrospray Mass Spectrometry. *Journal of Neurochemistry* **71**, 2465-2476 (1998). https://doi.org:https://doi.org/10.1046/j.1471-4159.1998.71062465.x

51 Yang, Y. *et al.* Altered succinylation of mitochondrial proteins, APP and tau in Alzheimer's disease. *Nature Communications* **13**, 159 (2022). https://doi.org:10.1038/s41467-021-27572-2

52 Liu, F., Iqbal, K., Grundke-Iqbal, I., Hart, G. W. & Gong, C.-X. O-GlcNAcylation regulates phosphorylation of tau: A mechanism involved in Alzheimer's disease. *Proceedings of the National Academy of Sciences* **101**, 10804-10809 (2004). https://doi.org:doi:10.1073/pnas.0400348101

53 Ksiezak-Reding, H., Liu, W.-K. & Yen, S.-H. Phosphate analysis and dephosphorylation of modified tau associated with paired helical filaments. *Brain Research* **597**, 209-219 (1992). https://doi.org:https://doi.org/10.1016/0006-8993(92)91476-U

54 Köpke, E. *et al.* Microtubule-associated protein tau. Abnormal phosphorylation of a non-paired helical filament pool in Alzheimer disease. *Journal of Biological Chemistry* **268**, 24374-24384 (1993). https://doi.org:https://doi.org/10.1016/S0021-9258(20)80536-5

55 Reynolds, C. H., Betts, J. C., Blackstock, W. P., Nebreda, A. R. & Anderton, B. H. Phosphorylation Sites on Tau Identified by Nanoelectrospray Mass Spectrometry. *Journal of Neurochemistry* **74**, 1587-1595 (2000). https://doi.org:https://doi.org/10.1046/j.1471-4159.2000.0741587.x

56 Yoshida, H. & Goedert, M. Sequential phosphorylation of tau protein by cAMP-dependent protein kinase and SAPK4/p38δ or JNK2 in the presence of heparin generates the AT100 epitope. *Journal of Neurochemistry* **99**, 154-164 (2006). https://doi.org:https://doi.org/10.1111/j.1471-4159.2006.04052.x

57 Cavallini, A. *et al.* An unbiased approach to identifying tau kinases that phosphorylate tau at sites associated with Alzheimer disease. *Journal of Biological Chemistry* **288**, 23331-23347 (2013).

58 Yoshiyama, Y. *et al.* Synapse loss and microglial activation precede tangles in a P301S tauopathy mouse model. *Neuron* **53**, 337-351 (2007).

59 Naseri, N. N. *et al.* Aggregation of mutant cysteine string protein-alpha via Fe-S cluster binding is mitigated by iron chelators. *Nature structural & molecular biology* **27**, 192-201 (2020). https://doi.org:10.1038/s41594-020-0375-y

60 Santhosh Kumar, S. *et al.* Sequential CRISPR screening reveals partial NatB inhibition as a strategy to mitigate alpha-synuclein levels in human neurons. *Science Advances* **10**, eadj4767 (2024).

61 Xu, T. *et al.* The Proteoform Landscape of Tau from the Human Brain. *Journal of Proteome Research*, 2916-2925 (2025). https://doi.org:10.1021/acs.jproteome.5c00139

62 Kafader, J. O. *et al.* Multiplexed mass spectrometry of individual ions improves measurement of proteoforms and their complexes. *Nature Methods* **17**, 391-394 (2020). https://doi.org:10.1038/s41592-020-0764-5

63 Lovestone, S., Hartley, C. L., Pearce, J. & Anderton, B. H. Phosphorylation of tau by glycogen synthase kinase-3β in intact mammalian cells: The effects on the organization and stability of microtubules. *Neuroscience* **73**, 1145-1157 (1996). https://doi.org:https://doi.org/10.1016/0306-4522(96)00126-1

64 Castoldi, M. & Popov, A. V. Purification of brain tubulin through two cycles of polymerization-depolymerization in a high-molarity buffer. *Protein Expr Purif* **32**, 83-88 (2003). https://doi.org:10.1016/s1046-5928(03)00218-3

65 Xie, Y. X. *et al.* Lysosomal exocytosis releases pathogenic α-synuclein species from neurons in synucleinopathy models. *Nature Communications* **13**, 4918 (2022).

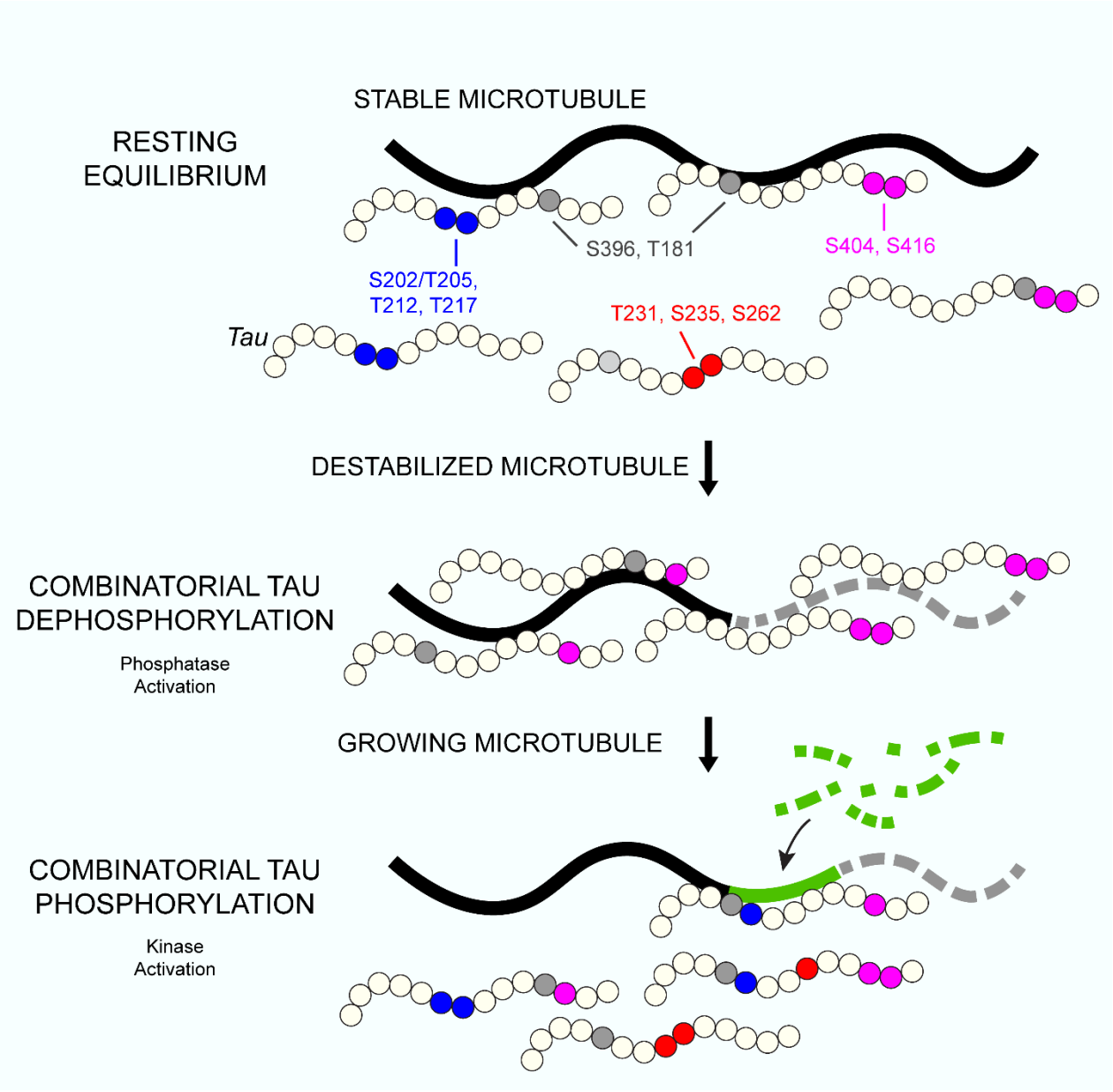

GRAPHICAL ABSTRACT

Schematic model of our findings: Tau phosphorylation is dynamically regulated in specific combinatorial patterns in response to shifting MT growth cycles.

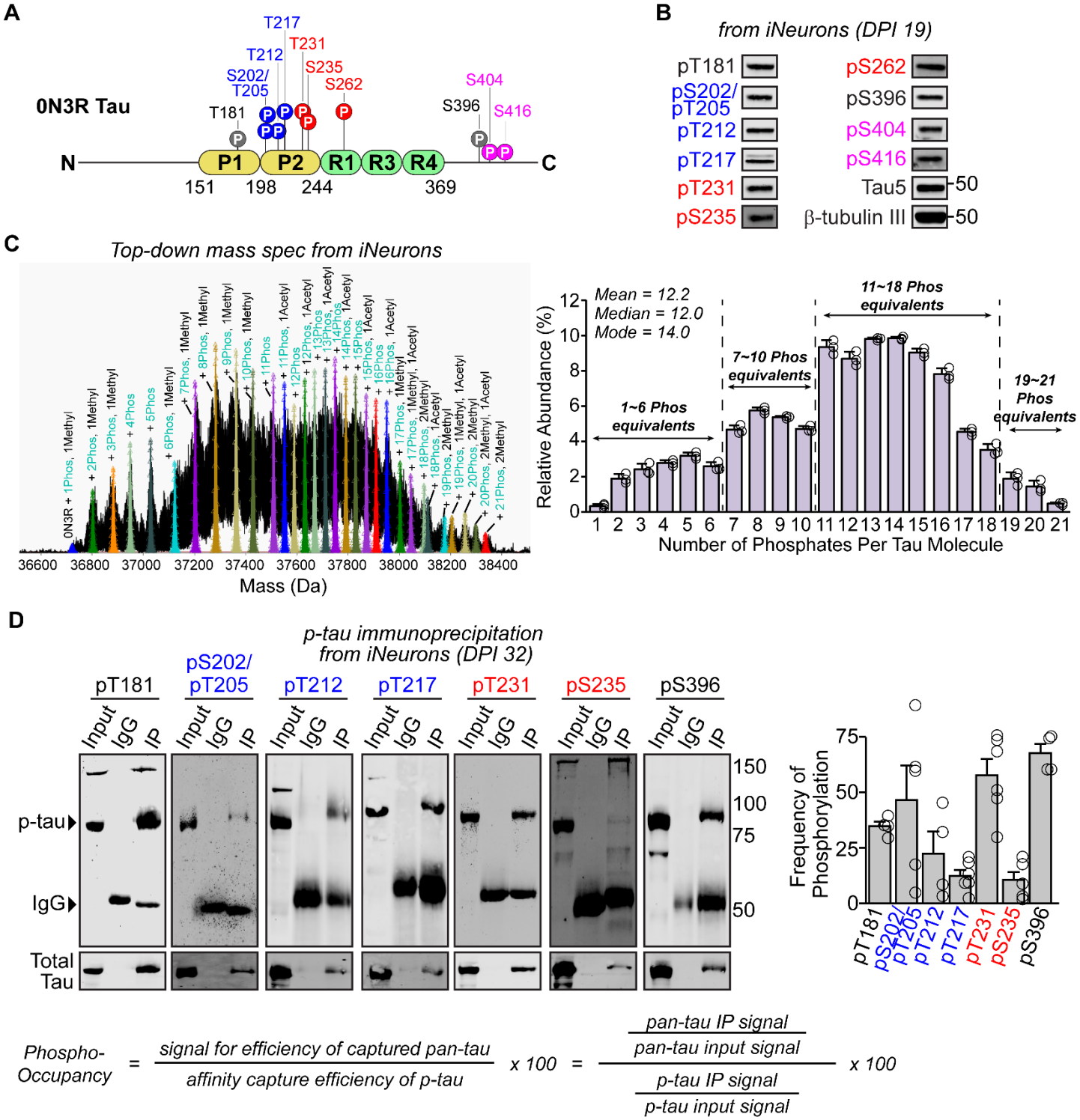

$$\text{Phospho-Occupancy} = \frac{\text{signal for efficiency of captured pan-tau}}{\text{affinity capture efficiency of p-tau}} \times 100 = \frac{\dfrac{\text{pan-tau IP signal}}{\text{pan-tau input signal}}}{\dfrac{\text{p-tau IP signal}}{\text{p-tau input signal}}} \times 100$$

e.g., calculations for a single replicate for pS396 immunoprecipitation

$$\frac{\dfrac{\text{pan-tau IP signal from pS396 IP}}{\text{pan-tau input from pS396 IP}}}{\dfrac{\text{p-tau IP signal from pS396 IP}}{\text{p-tau input signal from pS396 IP}}} \times 100 = \frac{\dfrac{1.12\times10^5}{2.33\times10^5 * \cancel{44.7}}}{\dfrac{4.28\times10^5}{5.28\times10^5 * \cancel{44.7}}} \times 100 = \frac{0.481}{0.811} \times 100 = \text{59.3\% of captured total tau was positive for pS396}$$

dil. factor

Figure 1 – Fetal tau is hyperphosphorylated in human iNeurons.

a) Schematic of the fetal human 0N3R tau isoform. Residue numbering is based on the 2N4R isoform, as is convention in

the field. The phospho-epitopes that were probed in this study in iNeurons are indicated and consistently color-coded throughout. **b)** P-tau was detected by immunoblot at the indicated epitopes in wildtype human iNeurons. Images are representative of numerous blots. **c)** Pan-tau was immunoprecipitated from iNeurons (*DPI 30*), and stoichiometries of phosphorylation events per tau protein were measured by top-down mass spectrometry with I^2MS technology, indicating up to 21 phosphates per tau protein. PTMs were assigned based on mass shifts of ~80 Da for phosphorylation, ~42 Da for acetylation and ~14 Da for methylation. The relative abundance of phosphate occupancy was calculated as a percentage of all detected 0N3R tau proteoforms. The annotated spectrum is representative of a single replicate of n=3 independent I^2MS injections. Quantifications represent mean ± STD for n=3 independent I^2MS injections. **d)** Tau^{KD} iNeurons were lentivirally transduced with $0N3R^{EGFP}$, and p-tau was then immunoprecipitated using the indicated p-tau antibody, separated by SDS-PAGE and immunoblotted against the indicated immunoprecipitated p-tau epitope and pan-tau (anti-Tau5 mouse for p-tau rabbit immunoprecipitations; anti-Tau5 rabbit for p-tau mouse immunoprecipitations). IgG control = anti-myc mouse monoclonal or anti-GAPDH rabbit polyclonal antibodies. Quantification of phospho-site abundance, described in the 'Methods' section, is representative of the average of two technical replicates for n=4 (pT181, pT212, pS396), n=5 (AT8) and n=6 (pT217, pT231, pS235) independent cultures and immunoprecipitations. An example of the back-calculation method is provided for a single replicate (out of 4 replicates) for quantification of phosphate occupancy at S396. All data are representative of mean ± SEM.

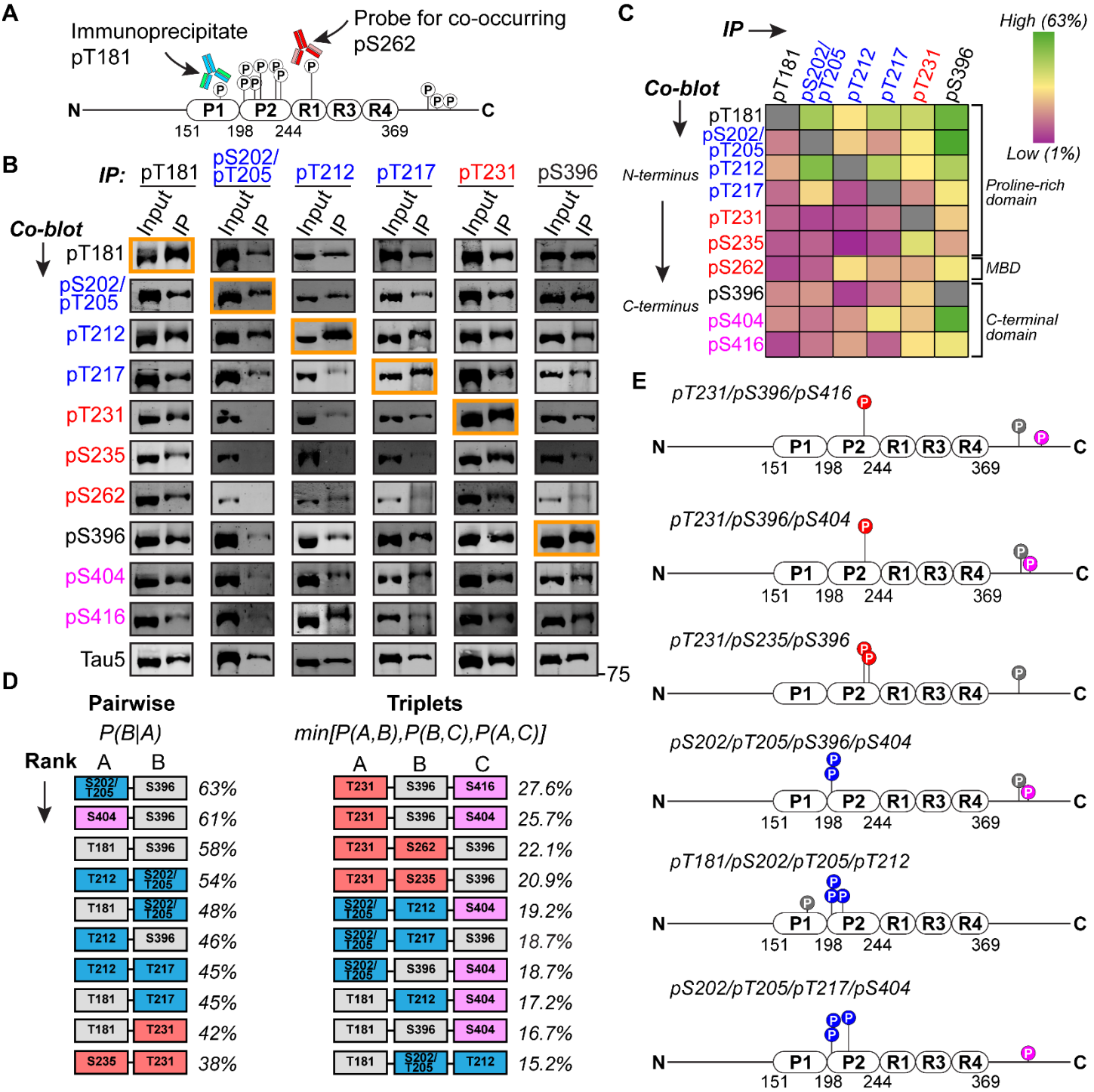

Figure 2: Phospho-epitopes are co-phosphorylated in specific patterns in iNeurons.

a) General workflow for p-tau immunoprecipitation from iNeurons under denaturing conditions, followed by blotting for co-occurring phospho-epitopes. **b)** Tau^{KD} iNeurons were lentivirally transduced with 0N3R^{EGFP}. P-tau was immunoprecipitated at 32 days post-induction, followed by separation by SDS-PAGE and immunoblotted against the indicated immunoprecipitated p-tau epitope and co-blotted at various p-tau epitopes. The immunoblot outlined in orange indicates the immunoprecipitated p-tau species in that given column of immunoblots. Blots are representative of n=4 (pT181, pT212, pS396), n=5 (pS202/pT205) and n=6 (pT217, pT231) independent cultures and immunoprecipitations. **c)** Heat map representing the quantification of phospho-site co-occurrence for each immunoprecipitated p-tau species, as described in the 'Methods' section. Green=high co-occurrence. Purple=low co-occurrence. Data is representative of n=4 (pT181, pT212,

pS396), n=5 (pS202/pT205) and n=6 (pT217, pT231) independent cultures and immunoprecipitations. **d)** The top 10 most common combinations of two and three co-occurring phospho-epitopes are ranked from top to bottom. For pairwise combinations, the percentages adjacent to each combination reflect the highest linkage for a given pair of phospho-epitopes. Combinations of three phospho-epitopes were predicted by minimum linkage analysis as described in the 'Methods' section. The percentages adjacent to each triplet represent the lowest co-occurrence probability between any of the three indicated epitopes. **e)** Schematic representation of several predicted combinatorial phospho-modifications to 0N3R tau in iNeurons.

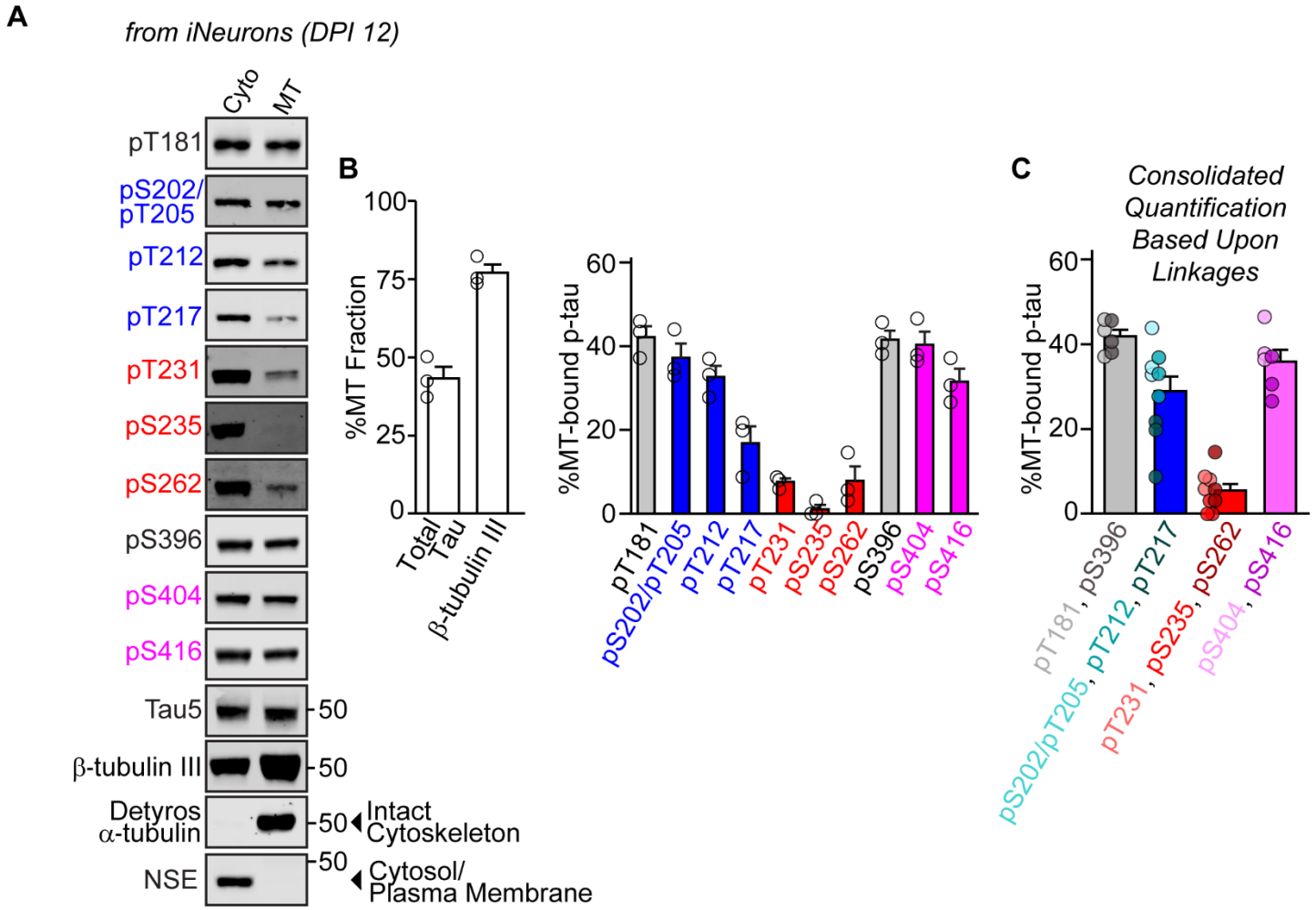

Figure 3: Specific tau phospho-epitopes are distinctly associated with cytosolic and MT-bound pools of tau.

a) MTs were fractionated from tau^{KD} iNeurons expressing 0N3R^{myc} at *DPI 12* (n=3 independent cultures, transductions and fractionations). SDS-PAGE followed by immunoblot was used to detect p-tau levels in cytosolic and MT-bound fractions. Separation of detyrosinated α-tubulin (MT fraction, only) from neuron-specific enolase (NSE), a cytosol-specific protein (cytosolic fraction, only), indicated successful separation of intact MTs from the cytosol. **b)** The amounts of pan-tau (anti-Tau5), β-tubulin III and p-tau that were found in the MT-bound fraction were quantified as a percentage of total protein (cytosolic + MT fractions) for each indicated target. **c)** A consolidated presentation of the quantifications in 'b' are presented based on the color-coded clusters that were defined in 'Figure 2d'. The quantifications for combined phospho-epitopes are as described: Gray (pT181, pS396): Blue (pS202/pT205, pT212, pT217): Red (pT231, pS235, pS262): Magenta (pS404, pS416). All data are representative of mean ± SEM.

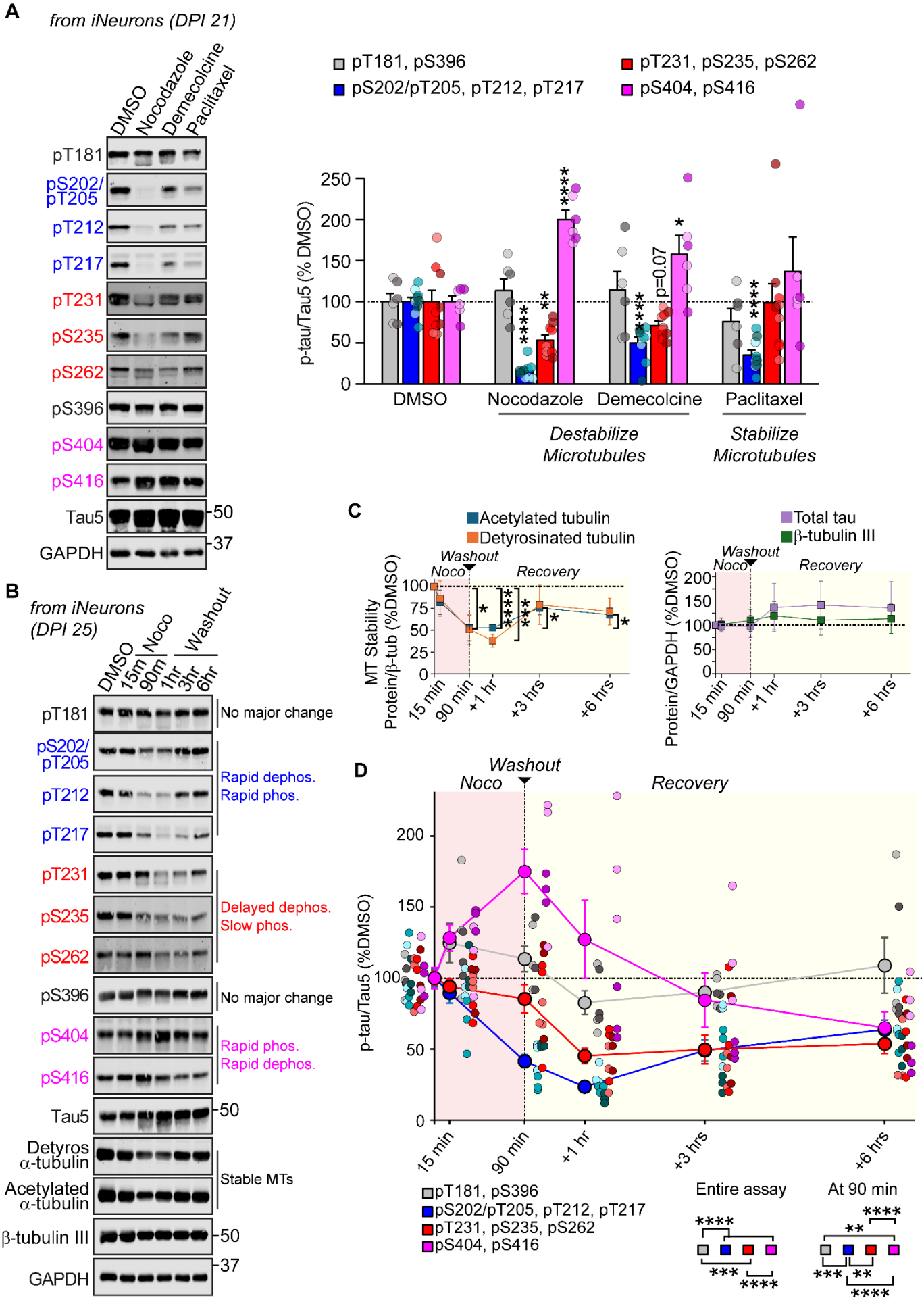
A
from iNeurons (DPI 21)
DMSO
Nocodazole
Demecolcine
Paclitaxel
pT181
pS202/pT205
pT212
pT217
pT231
pS235
pS262
pS396
pS404
pS416
Tau5
GAPDH
50
37
pT181, pS396
pS202/pT205, pT212, pT217
pT231, pS235, pS262
pS404, pS416
p-tau/Tau5 (% DMSO)
p=0.07
DMSO
Nocodazole
Demecolcine
Paclitaxel
Destabilize Microtubules
Stabilize Microtubules
B
from iNeurons (DPI 25)
DMSO
15m
90m
1hr
3hr
6hr
Noco
Washout
No major change
Rapid dephos.
Rapid phos.
Delayed dephos.
Slow phos.
Rapid phos.
Rapid dephos.
Detyros α-tubulin
Acetylated α-tubulin
Stable MTs
β-tubulin III
C
Acetylated tubulin
Detyrosinated tubulin
Washout
Noco
Recovery
MT Stability
Protein/β-tub (%DMSO)
15 min
90 min
+1 hr
+3 hrs
+6 hrs
Total tau
β-tubulin III
Protein/GAPDH (%DMSO)
D
Washout
Noco
Recovery
p-tau/Tau5 (%DMSO)
pT181, pS396
pS202/pT205, pT212, pT217
pT231, pS235, pS262
pS404, pS416
Entire assay
At 90 min

189

190 **Figure 4: Phospho-sites throughout tau are differentially regulated by MT integrity.**

191 **a)** iNeurons (*DPI 21*) were treated with either DMSO (control), nocodazole (10 μM), demecolcine (1 μM) or paclitaxel (10
192 μM) for 90 minutes to manipulate the cytoskeleton. Samples were separated by SDS-PAGE followed by anti-p-tau
193 immunoblot. P-tau levels were quantified and normalized to pan-tau (anti-Tau5) for each treatment and then normalized to
194 DMSO-treated samples (control). N=3 independent cultures and treatments per group. All data are representative of mean
195 ± SEM. *P<0.05; **P<0.01; ****P<0.0001 by Student's t-test. For **b-d)** iNeurons (*DPI 25*) were treated with either DMSO
196 (control) or 10 μM nocodazole for either 15 min, 90 min, or 90 min followed by nocodazole washout and recovery for 1 hour,
197 3 hours or 6 hours. **b)** Samples were harvested for SDS-PAGE followed by immunoblot against the indicated proteins. N=3
198 independent cultures and treatments per group. **c)** Quantification of 'b' for MT stability as measured by changes to
199 detyrosinated α-tubulin and K40 acetylated α-tubulin during nocodazole treatment and washout. Total (pan) tau and β-
200 tubulin III levels were not significantly impacted throughout the assay. **d)** Quantification of 'b' for p-tau. **P<0.01; ***P<0.001;
201 ****P<0.0001 by post-hoc Tukey's HSD test.

202

203

204

205

206

207

208

209

210

211

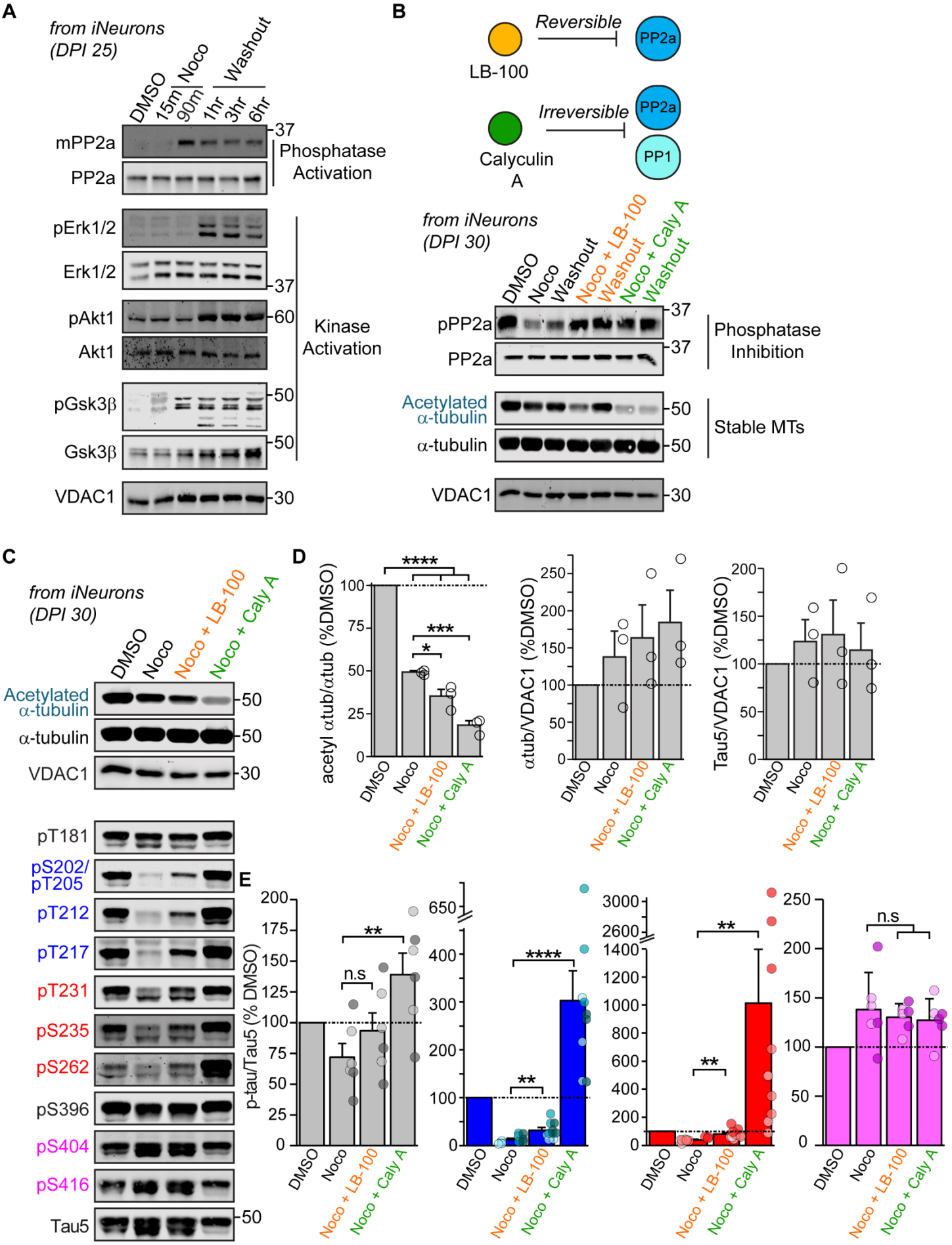
A
from iNeurons
(DPI 25)
DMSO
Noco
15m
90m
Washout
1hr
3hr
6hr
mPP2a
PP2a
Phosphatase Activation
pErk1/2
Erk1/2
pAkt1
Akt1
pGsk3β
Gsk3β
Kinase Activation
VDAC1
37
60
50
30
B
Reversible
LB-100
PP2a
Irreversible
Calyculin A
PP1
from iNeurons
(DPI 30)
Noco + LB-100
Noco + Caly A
pPP2a
Phosphatase Inhibition
Acetylated α-tubulin
α-tubulin
Stable MTs
C
pT181
pS202/pT205
pT212
pT217
pT231
pS235
pS262
pS396
pS404
pS416
Tau5
D
acetyl αtub/αtub (%DMSO)
αtub/VDAC1 (%DMSO)
Tau5/VDAC1 (%DMSO)
****
***
*
E
p-tau/Tau5 (% DMSO)
n.s
**

212

Figure 5 – Tau dephosphorylation by PP2a is necessary to stabilize shrinking MTs.

a) iNeurons (*DPI 25*) were treated with either DMSO (control) or 10 μM nocodazole for either 15 min, 90 min, or 90 min followed by nocodazole washout and recovery for 1 hour, 3 hours or 6 hours. PP2a activation was measured by methylation at Leu309. Kinase activation was measured by phosphorylation against Erk1/2 (T202/T204), Akt1 (S473) and GSK3β (Y216). Blots are representative of n=3 independent treatments. **b)** iNeurons (*DPI 30*) were simultaneously treated with nocodazole and the indicated PP2a inhibitors (LB-100 at 20 μM; Calyculin A at 20 nM). The nocodazole and phosphatase inhibitors were washed out and neurons were allowed to recover for 3 hours. Successful PP2a inhibition was determined by anti-phosho-PP2a (Y307) immunoblot. Changes to MT stability were determined by anti-acetylated-α-tubulin (K40) immunoblot. Blots are representative of n=4 independent treatments. For **c-e**, iNeurons (*DPI 30*) were treated with either DMSO (control), 10 μM nocodazole, or 10 μM nocodazole supplemented with either LB-100 (20 μM) or Calyculin A (20 nM) for 90 min. N=3 independent treatments. **c)** Representative immunoblots are shown for the indicated proteins and p-tau epitopes. **d)** As in 'b', quantification of changes to MT stability by immunoblot against α-tubulin acetylated at K40. No significant changes were detected to total α-tubulin or pan-tau (anti-Tau5) levels. **e)** As in 'd', changes to p-tau were measured by immunoblot against the indicated phospho-epitopes. P-tau levels were normalized to pan-tau (anti-Tau5) for each sample. N.S.=not significant. **P<0.01; ***P<0.001; ****P<0.0001 by Student's t-test. All data are representative of mean ± SEM.

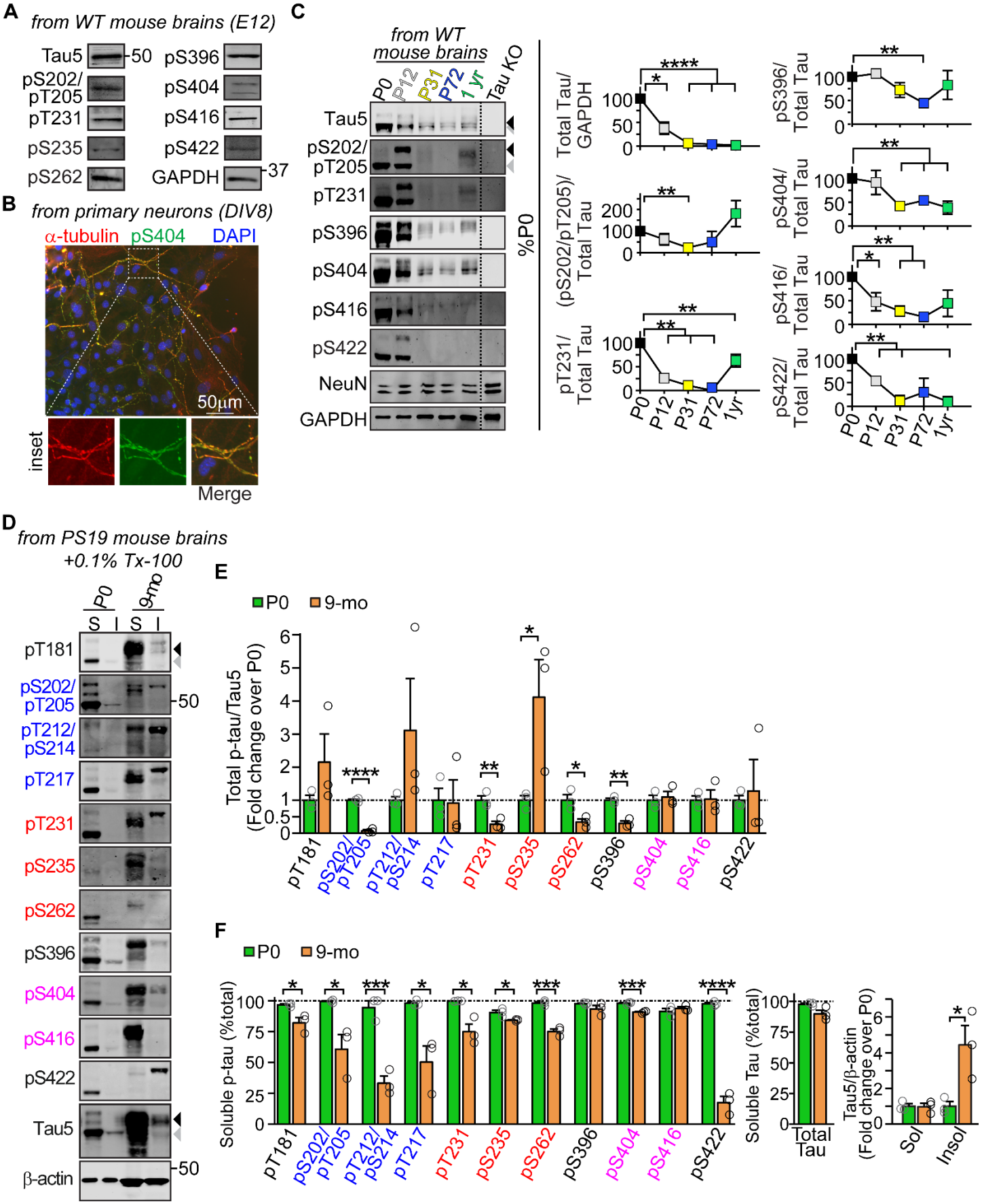

Figure 6: p-tau is abundant and highly soluble in developing mouse brains.

a) Brains were collected from wildtype mice on embryonic day 12 (E12). Following separation by SDS-PAGE, pan-tau (anti-

Tau5) and p-tau sites were detected by immunoblot at the indicated epitopes. Immunoblots are representative of 6 embryonic mouse brains. **b)** Tau phosphorylated at S404 (green) colocalized with MT protein α-tubulin (red) in wildtype primary mouse neurons at *DIV*8. **c)** Wildtype mouse brains were collected at post-natal days 0, 12, 31, 72 and at 1 year, and from tau$^{-/-}$ mice (P60). Pan-tau (anti-Tau5) and p-tau were detected by immunoblot. Pan-tau levels were normalized to GAPDH, and p-tau levels were normalized to pan-tau at each time point. The band shift from the gray arrowhead to the black arrowhead represents the isoform shift from 3R to 4R tau, respectively. Immunoblots and quantifications are representative of n=3 littermates. For **d-f**, PS19 mouse brains were collected at post-natal days 0 and at 9 months. N=3 littermates per time point. The band shift between P0 and 9 months represents 0N3R mouse tau (gray arrowhead) and 1N4R human tau (black arrowhead). **d)** Triton-X solubility from PS19 mouse brains was used to separate [S]oluble from [I]nsoluble p-tau, followed by immunoblot. **e)** Total p-tau levels (soluble + insoluble) were quantified and normalized to pan-tau (anti-Tau5) at each time point and represented as a fold-change of P0 levels. **f)** P-tau solubility was quantified as a percentage of total p-tau (soluble + insoluble) for each epitope at each time point. Pan-tau (anti-Tau5) solubility was quantified by Tau5/β-actin as a fold-change of P0 levels for both the soluble and insoluble fractions. Immunoblots and quantifications are representative of n=3 littermates. All data are representative of mean ± SEM. *P<0.05; **P<0.01; ***P<0.001; ****P<0.0001 by Student's t-test.

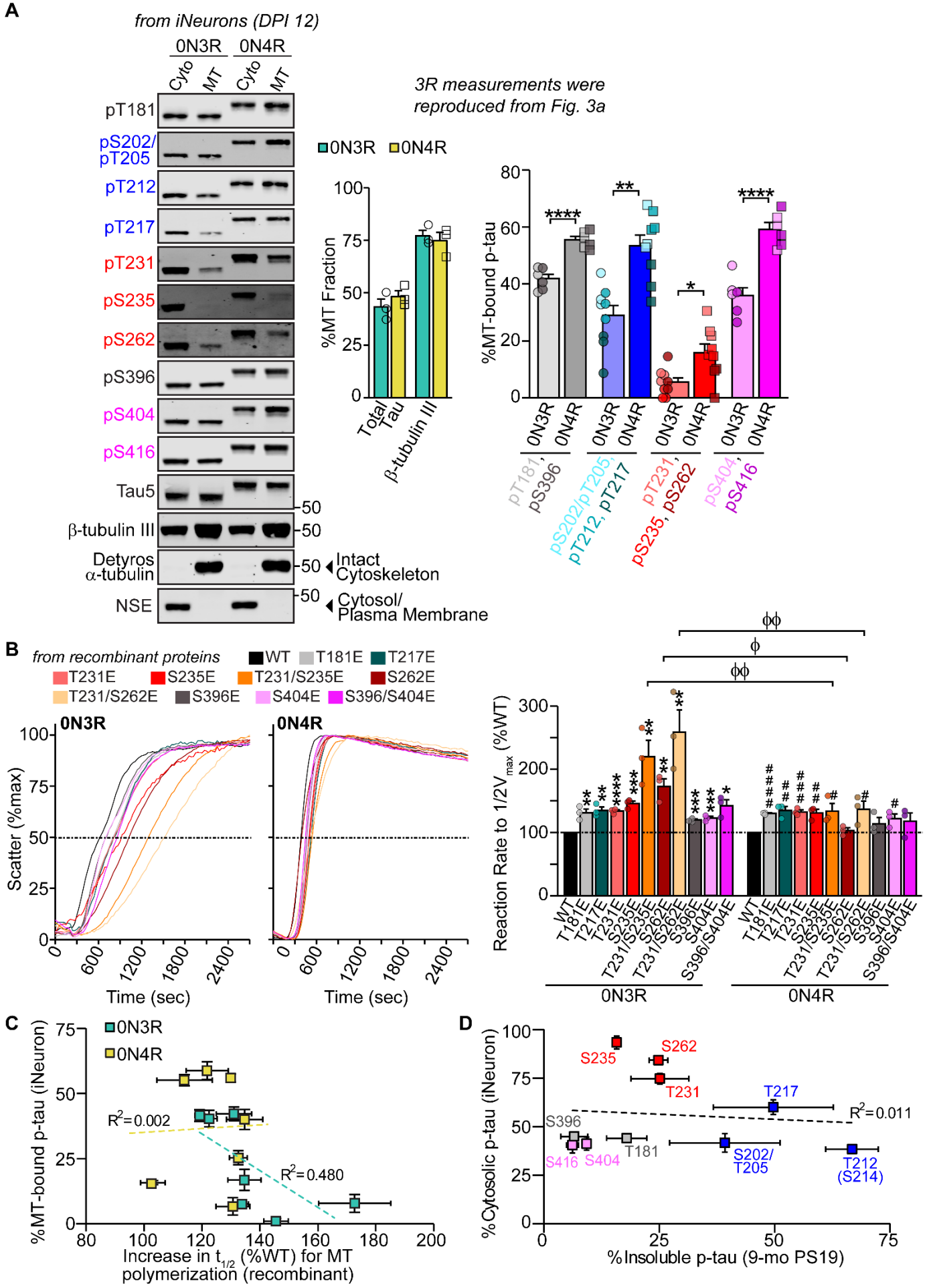
A
from iNeurons (DPI 12)
0N3R
0N4R
Cyto
MT
Cyto
MT
pT181
pS202/ pT205
pT212
pT217
pT231
pS235
pS262
pS396
pS404
pS416
Tau5
β-tubulin III
Detyros α-tubulin
NSE
50
Intact Cytoskeleton
Cytosol/ Plasma Membrane
3R measurements were reproduced from Fig. 3a
0N3R
0N4R
%MT Fraction
Total Tau
β-tubulin III
%MT-bound p-tau
pT181, pS396
pS202/pT205, pT212, pT217
pT231, pS235, pS262
pS404, pS416
B
from recombinant proteins
WT
T181E
T217E
T231E
S235E
T231/S235E
S262E
T231/S262E
S396E
S404E
S396/S404E
0N3R
0N4R
Scatter (%max)
Time (sec)
Reaction Rate to 1/2V max (%WT)
C
%MT-bound p-tau (iNeuron)
R2=0.002
R2=0.480
Increase in t1/2 (%WT) for MT polymerization (recombinant)
D
%Cytosolic p-tau (iNeuron)
S235
S262
T231
T217
S396
T181
S416
S404
S202/ T205
T212 (S214)
R2=0.011
%Insoluble p-tau (9-mo PS19)

Figure 7: Phosphorylation is more disruptive to 3R than 4R tau's interaction with MTs.

a) MTs were fractionated from tau^{KD} iNeurons expressing 0N4R^{myc} at *DPI 12* (n=3 independent cultures, transductions and fractionations), as in Figure 3a. The measurements for 0N3R were re-plotted from Figure 3a to facilitate comparison. SDS-PAGE followed by immunoblot was used to detect p-tau levels in cytosolic and MT-bound fractions. Separation of detyrosinated α-tubulin (MT fraction, only) from neuron-specific enolase (NSE), a cytosol-specific protein (cytosolic fraction, only), indicated successful separation of intact MTs from the cytosol. The percentage of p-tau that was found in the MT-bound fraction was quantified as a percentage of total p-tau (cytosolic + MT fractions) for each phospho-site. **b)** MT polymerization was detected *in vitro* by light scatter at 340 nm for recombinant wildtype 0N3R, wildtype 0N4R, or phospho-mimics of each at the indicated sites. The reaction mixture (20 μM soluble tubulin + 10 μM recombinant tau in BRB80 buffer) was supplemented with 1 mM DTT (final), initiated by addition of 1 mM GTP (final) at 37C and monitored for 45 minutes on a spectrophotometer. N=3 independent polymerization reactions for each tau variant. Quantification of the change in the reaction rate to 50% V_{max} for each phospho-mimic was compared to wildtype tau for either 0N3R or 0N4R isoforms. For 0N3R: *P<0.05; **P<0.01; ***P<0.001; ****P<0.0001 by Student's t-test. For 0N4R: #P<0.05; ##P<0.01; ###P<0.001; ####P<0.0001 by Student's t-test. For comparison of 0N3R to 0N4R: ΦP<0.05; ΦΦP<0.01 by Student's t-test. All data are representative of mean ± SEM. **c)** The percentage of MT-bound 0N3R and 0N4R p-tau from iNeurons (from Fig. 7a) was plotted alongside the increase in $t_{1/2}$ rate of MT polymerization by tau phospho-mimics compared to WT (from Fig. 7b), for epitopes T181, T217, T231, S235, S262, S396 and S404. **d)** The percentage of cytosolic 0N4R p-tau from iNeurons (from Fig. 7a), was plotted alongside the percentage of insoluble p-tau from 9-month-old PS19 mouse brains (from Fig. 6F). Note that the measurements for phospho-epitope T212 (MT fractionation from iNeurons) were paired with T212/S214 (solubility from PS19 mouse brains).

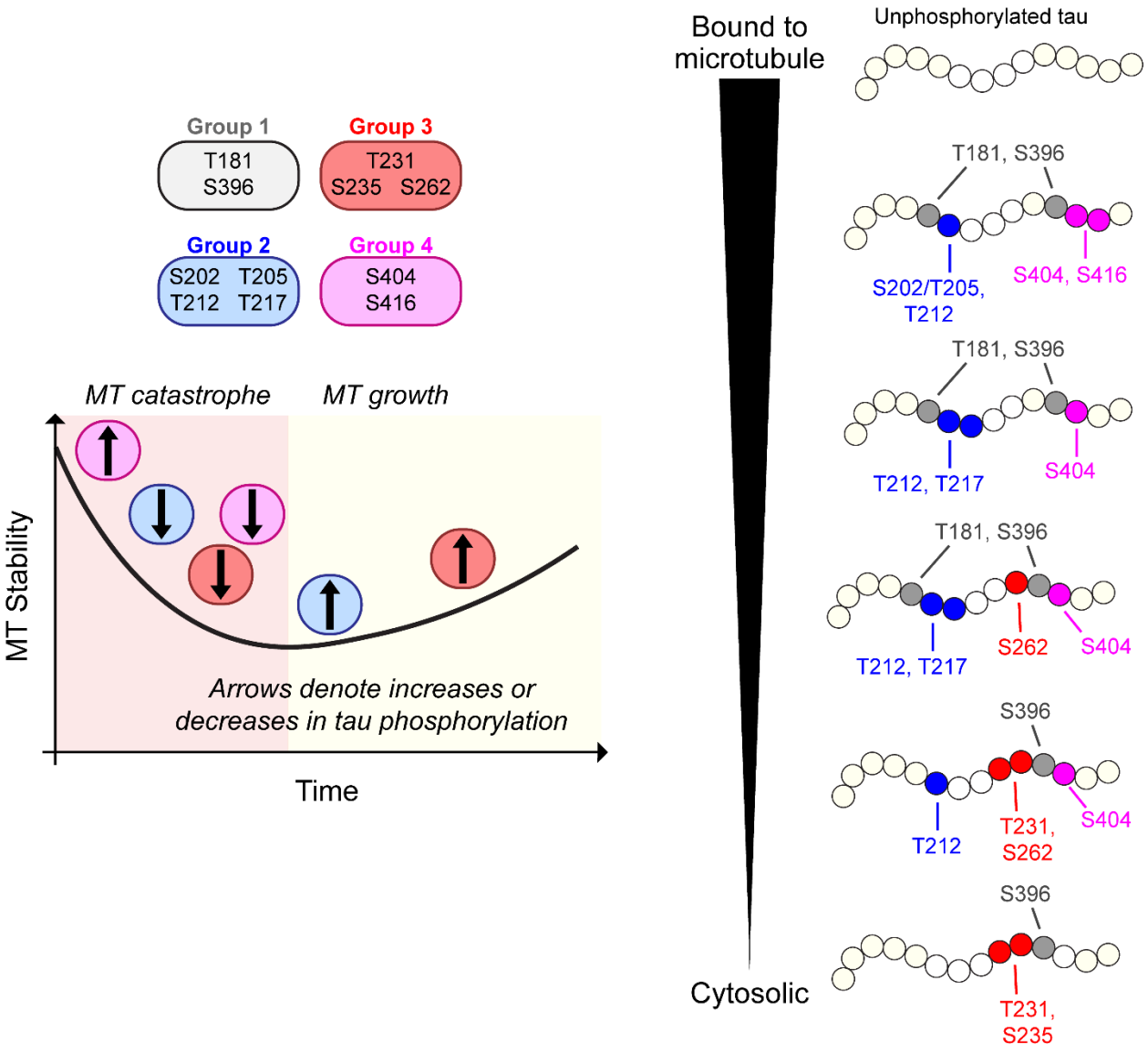

Figure 8: Schematic summary

Temporal changes to site-specific phosphorylated occur in specific combinations in response to MT collapse and growth. Based on co-occurrence linkage of phospho-epitopes, fractionation of MT-bound and cytosolic proteins, and changes to site-specific phosphorylated during MT collapse and growth, we present predictions of the likelihood that certain combinatorial phospho-modifications to tau are found bound to or dissociated from MTs.